Research Square

Preprints are preliminary reports that have not undergone peer review.
They should not be considered conclusive, used to inform clinical practice,
or referenced by the media as validated information.

Recharge sources, hydrochemical evolution, and health risks of groundwater and geothermal water in the Guangdong-Fujian coastal region, southeastern China

Ruibin Li
United Laboratory of High-Pressure Physics and Earthquake Science, Institute of Earthquake Forecasting, China Earthquake Administration

Xiaocheng Zhou
zhouxiaocheng188@163.com

United Laboratory of High-Pressure Physics and Earthquake Science, Institute of Earthquake Forecasting, China Earthquake Administration

Fenna Zhang
Observation and Research Station of Tianjin Low-Medium Temperature Geothermal Resources, Tianjin Municipal Bureau of Planning and Natural Resources

Bingyu Yao
China University of Geosciences

Zhaojun Zeng
China University of Geosciences

Yuwen Wang
China University of Geosciences

Han Yan
China University of Geosciences

Jin Liu
Guangdong earthquake agency

Jiyu Li
Fujian earthquake agency

Miao He
United Laboratory of High-Pressure Physics and Earthquake Science, Institute of Earthquake Forecasting, China Earthquake Administration

Jiao Tian
United Laboratory of High-Pressure Physics and Earthquake Science, Institute of Earthquake Forecasting, China Earthquake Administration

Chuanyong Wang

Diligence Markes Leading Manufacturing Center, NO.1 Mud Logging Branch Company, BoHai Drilling Company

---

Article

Keywords: Thermal springs, Trace element contamination, Manganese enrichment, Self-organizing map, Health risk assessment, Southeast China

Posted Date: August 10th, 2026

DOI: https://doi.org/10.21203/rs.3.rs-10046101/v1

License: This work is licensed under a Creative Commons Attribution 4.0 International License. Read Full License

Additional Declarations: No competing interests reported.

Recharge sources, hydrochemical evolution, and health risks of groundwater and geothermal water in the Guangdong-Fujian coastal region, southeastern China

Ruibin Li[1], Xiaocheng Zhou[1,2*], Fenna Zhang[3,4*], Bingyu Yao[2], Zhaojun Zeng[5], Yuwen Wang[2],Han Yan[2], Jin Liu[6], Jiyu Li[7], Miao He[1], Jiao Tian[1], Chuanyong Wang[8]

[1]United Laboratory of High-Pressure Physics and Earthquake Science, Institute of Earthquake Forecasting, China Earthquake Administration, Beijing 100036

[2]School of Earth Sciences and Resources, China University of Geosciences, Beijing 100083, China

[3]Observation and Research Station of Tianjin Low-Medium Temperature Geothermal Resources, Tianjin Municipal Bureau of Planning and Natural Resources, Tianjin 300250, China

[4]Tianjin Geothermal Exploration and Development-Designing Institute, Tianjin 300250, China

[5]School of Water Resources and Environment, China University of Geosciences, Beijing 100083, China

[6]Guangdong earthquake agency, Guangdong, 510070, China

[7]Fujian earthquake agency, Fuzhou, 350025

[8]Diligence Markes Leading Manufacturing Center, NO.1 Mud Logging Branch Company, BoHai Drilling Company, Tianjin 300280, China

Corresponding author: Xiaocheng Zhou (zhouxiaocheng188@163.com, ying-ying22@163.com)

Keywords Thermal springs, Trace element contamination, Manganese enrichment, Self-organizing map, Health risk assessment, Southeast China

Abstract

Cold and thermal groundwater are vital resources in coastal regions, yet their contrasting hydrochemical characteristics may influence drinking suitability and health risks. This study analyzed 124 groundwater samples from Guangdong and Fujian provinces (94 newly collected, 30 from literature) for major/trace elements and stable isotopes. Using World Health Organization (WHO) guidelines, Chinese standards (GB 5749-2022, GB/T 14848-2017), and methods including self-organizing map with K-means algorithm (SOM-KM), principal component analysis (PCA), water quality index (WQI), and human health risk assessment (HHRA), we assessed water quality and sources. The results show that the dominant recharge is meteoric water, with Na-Cl and Na-HCO_3 types prevailing. Although the quality of most water is acceptable, groundwater in Chagan Town (located at the border of Guangdong and Fujian provinces) and Zhongshan City fails to meet drinking standards and carries considerable non carcinogenic risks. Manganese enrichment controlled by lithology and redox conditions constitutes the primary health hazard. Exclusive dependence on the WQI index may underestimate the risk levels of specific elements. Hence, integrating multiple valid analyses to conduct comprehensive evaluation is essential for groundwater management.

Introduction

Groundwater and geothermal water are important natural resources in coastal regions, which support domestic supply, tourism, agriculture, and energy utilization[1–11]. As a direct natural carrier of geothermal energy, geothermal water has been widely used for heating, bathing, greenhouse cultivation, and other low- to medium-enthalpy applications in many parts of the world[12,13]. In densely populated and economically developed regions, such as southeastern China, groundwater also plays a critical role in sustaining regional water security[14,15]. Compared with shallow cold groundwater, thermal groundwater generally experiences deeper circulation which results in higher temperatures, and stronger water-rock interaction. This characteristic leads to distinct hydrochemical and isotopic characteristics[16,17]. Understanding the differences and linkages between cold and thermal groundwaters is therefore important for both resource utilization and water safety assessment.

Previous studies have extensively discussed hydrochemical characteristics of groundwater, geothermal resource utilization and hot spring systems under diverse geological environments[18,19]. However, most studies only focus on a single type of groundwater or local geothermal system, while systematic comparative research on cold and hot groundwater within analogous regions remains scarce[20–23]. In southeastern coastal China, groundwater chemistry is often influenced by multiple interacting processes[24–26]. These processes create compositional disparities in groundwater and complicate the identification of the dominant controls on hydrochemical differentiation.

Investigation of hydrochemical evolution serves as a prerequisite for assessing groundwater drinking suitability and associated health risks[27,28]. Natural processes and anthropogenic factors can enrich major ions and potentially toxic trace elements, thereby impairing groundwater quality[29–33]. In complex groundwater systems, use conventional hydrochemical diagrams alone is insufficient to resolve sample heterogeneity and controlling mechanisms[34,35]. Multivariate statistical approaches, such as SOM-KM and PCA, are useful for identifying hydrochemical groupings and disentangling the dominant factors controlling groundwater evolution[36,37]. For water quality assessment, WQI is widely applied to evaluate the overall

suitability of groundwater for drinking purposes, whereas HHRA delivers refined assessments of non-carcinogenic risks posed by individual elements[38–40].

Guangdong and Fujian Provinces on the southeast coast of China are characterized by extensively exploited groundwater and the coexistence of cold and hot groundwater under complex geological and hydrogeological settings[15,41,42]. This regional setting provides a suitable framework for investigating groundwater differentiation, hydrochemical evolution, and water safety in areas where cold and thermal groundwaters coexist[43]. Therefore, this study aims to: (1) characterize the hydrochemical and isotopic features of cold and thermal groundwaters; (2) identify the dominant processes controlling groundwater hydrochemical differentiation in the study area; (3) evaluate groundwater drinking suitability using WQI and assess localized human health risks using HHRA; and (4) examine the complementary roles of WQI and HHRA in groundwater safety assessment.

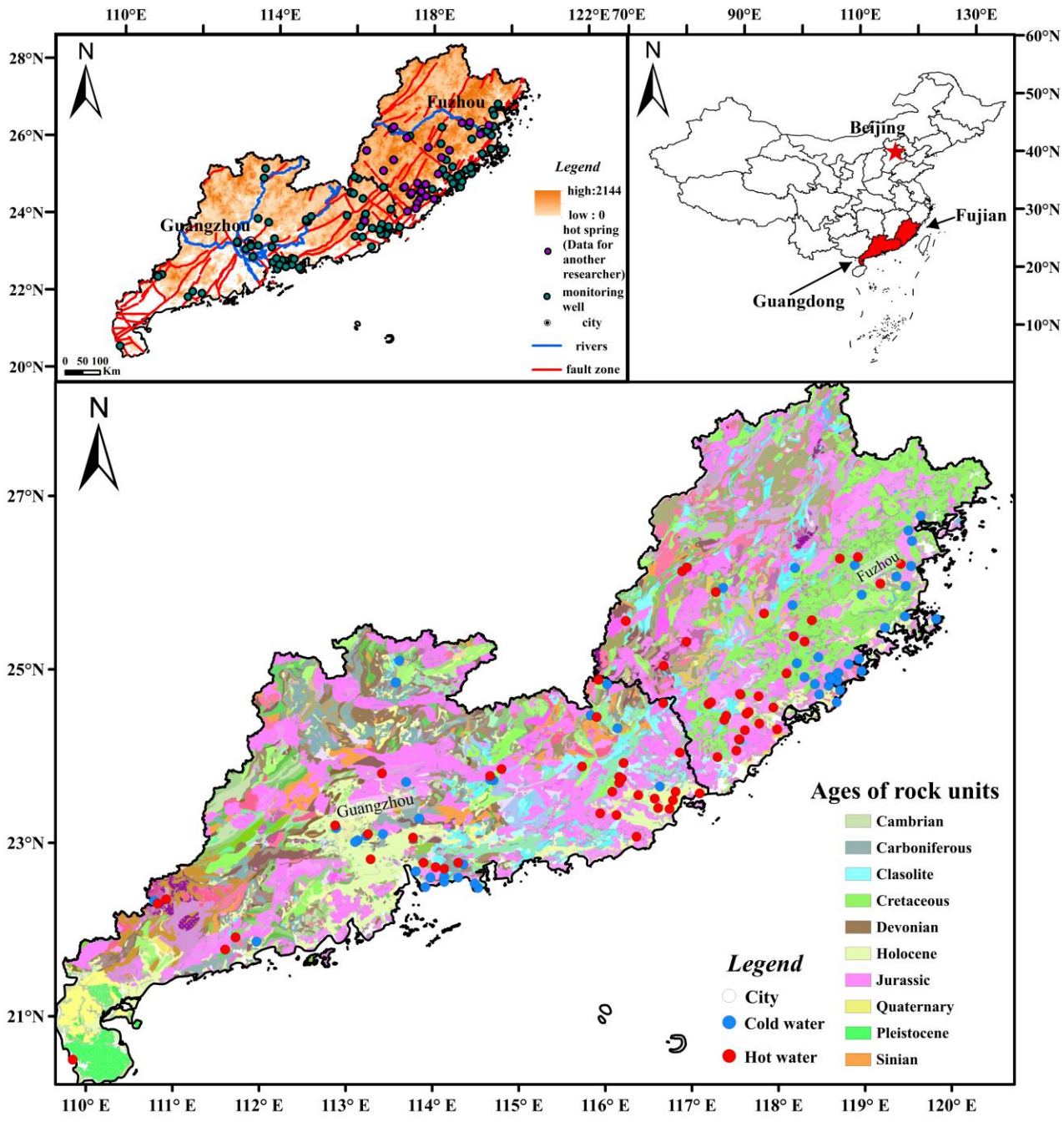


Figure 1. Study area and locations of water samples.

Study area

Geographic and climatic setting

The study area includes Guangdong and Fujian provinces along the southeastern coast of China, extending from 109°45′ to 120°43′E and from 20°09′ to 28°18′N, with a total area of approximately 302,800 km^2 (source: Ministry of Natural Resources of China). Although Guangdong and Fujian are geographically adjacent, they exhibit significant disparities in

geomorphic characteristics. Guangdong features the Pearl River Delta plains and Nanling hilly areas, while Fujian is dominated by mountains and hills, with local karst landscapes and coastal sedimentary plains. Both provinces have relatively high annual precipitation, generally exceeding 1500 mm and strongly influenced by the monsoon climate. Rainfall is mainly concentrated in summer, accounting for approximately 80% of the annual total[44,45].

Geological and hydrogeological setting

Guangdong and Fujian provinces are located along the southeastern margin of the South China Block, having undergone several phases of tectonic movements, including the Tethys Ocean's closure, the Pacific Plate's westward subduction, and the South China Sea's expansion[19,46,15]. The Jiangshan-Shaoxing Fault and Pingxiang-Yushan Fault divide the South China Block into the Yangtze Craton and the Cathaysia Block. Since the Archean, the block has undergone intense modification by the Caledonian orogeny in the Paleozoic, the Indosinian orogeny in the Mesozoic, as well as extensional rifting during the Yanshanian period[47–49]. Granites and intermediate-acidic volcanic rocks are widely distributed in the area. Some granites are characterized by relatively high radiogenic heat production and favorable thermal conductivity. Under suitable conditions, such as well-developed fractured granite reservoirs and favorable thermal insulation by cap rocks, geothermal systems may develop[50,51,37,52,53]. Since the Proterozoic, some granites have been distributed inland, which is opposite to the migration direction of the tectonic active belts, while the overall tectonic active belts have migrated southeastward toward the ocean[46]. This tectonic evolution has resulted in the extensive development of multi-stage composite granites[54]. Meanwhile, during deep circulation, geothermal fluids may undergo strong water-rock interaction with host rocks, primarily granites, which can alter the chemical composition of geothermal fluids and contribute to distinct hydrochemical characteristics[55].

Groundwater in the study area consists of three main types: pore water in loose sediments, bedrock fracture water in granites and volcanic rocks, and karst water in carbonate rocks[56]. Bedrock fracture water mainly occurs in tectonic and weathered fractures of Yanshanian granites, rhyolites, basalts, and metamorphic rocks, which are widely distributed in Guangdong and Fujian [57]. Pore water in loose sediments is mainly distributed in the Pearl River Delta, the lower Minjiang River, and coastal plains, occurring in Quaternary alluvial-proluvial and marine gravel, sand, and silt layers[58,59]. Pore water can be further divided into shallow pore water (0-30m) and medium-deep pore water (50-200m). Shallow aquifers are characterized by shallow burial, relatively good permeability, and easy exploitation, and they serve as important water supply aquifers in the region[60]. Carbonate karst water is mainly distributed in northern Guangdong, the Guanghua Basin, and southwestern Fujian, hosted in dissolution fractures, pores, caves, and underground conduit systems of Carboniferous, Permian, and Devonian limestones and dolomites. Controlled by dissolution and tectonism, karst groundwater generally has high but spatially uneven water yield[61,62].

Overall, the coexistence of diverse aquifer types, widespread granitic and volcanic rocks, active fault systems, and intensive coastal development makes Guangdong and Fujian suitable areas for investigating the hydrochemical differentiation and water quality of cold and thermal groundwaters[63].

Materials and methods

Sample collection and data sources

In this study, a total of 124 water samples were used in this study, including 94 newly collected samples and 30 samples compiled from previously published data[64] (Fig.1). Among the 94 newly collected samples, 84 were collected from monitoring wells and 10 from hot springs. The 30 literature-derived samples were all hot spring samples. Therefore, the dataset included both cold groundwater and thermal groundwater samples, providing a basis for comparing their hydrochemical characteristics.

Chemical and isotopic analyses

All collected water samples were delivered to the laboratory for experimental analysis, with particular attention paid to their hydrogeochemical signatures. Major anions and cations were determined using the Thermo Scientific Dionex AQUION ion chromatography system. The instrument was equipped with an AS40 autosampler provided by the Key Laboratory of Earthquake Prediction, China Earthquake Administration, with a detection limit of 0.01 mg/L. $CO_3^{2-}$and HCO_3^- were measured by titration with a ZDJ-3D automatic potentiometric titrator using 0.05 mol/L hydrochloric acid. Standard reference samples were tested prior to each batch of water samples for chromatographic calibration, with deviations controlled within ±2‰. All trace elements were determined using an Agilent 8900 ICP-MS instrument. The detection limits for Ba, Mn, Sr, Li, As, Fe, and B are 0.2, 0.12, 0.29, 0.33, 0.12, 0.82 and 1.25 μg/L, respectively. Since the study area is adjacent to the coast, a charge balance error within ±10% for anions and cations is regarded as acceptable for samples potentially affected by seawater intrusion[65–67]. The formula is expressed as follows:

$$\mathrm{ib}(\%)=\frac{\sum\text{cations}-\sum\text{anions}}{0.5(\sum\text{cations}+\sum\text{anions})}\times 100$$

pH and conductivity were measured by the Orion Star A325 portable meter. Stable hydrogen and oxygen isotopes were analyzed with a Picarro L2140-I liquid and vapor water isotope analyzer. All isotope measurements were referenced to the Vienna Standard Mean Ocean Water (V-SMOW). The $\delta^{18}O$ and δD values were measured with an accuracy of ±0.2‰ (2SD) and ±1‰ (2SD), respectively.

Data processing and statistical methods

Statistical analysis approaches consist of conventional multivariate statistics and intelligent analytical methods like SOM. Multivariate statistical techniques are capable of effectively addressing complex data in hydrochemical analysis and facilitating the identification of correlations among water quality indicators[36,68]. By means of techniques like dimensionality reduction, clustering, and regression analysis, these approaches can disclose the primary driving factors underlying water quality variations, thereby offering scientific evidence for water quality management and pollution source identification.

SOM is a kind of artificial neural network. It acts as an unsupervised learning algorithm dedicated to clustering tasks and high-dimensional visualization[69]. The SOM method projects high-dimensional complex data into a low-dimensional hexagonal neuron space based on similar data features, so as to realize the visualization of topological characteristics[69–72]. This study adopts

Eq.(1) to determine the optimal number of neurons for the SOM model. M donates the total neurons. N is defined as the number of input samples.

$$m=5\sqrt{n} \quad (1)$$

Yet the SOM model has inherent limitations: a single standalone model cannot determine the optimal number of clusters, which may compromise classification accuracy. To address this drawback, the K-means algorithm is adopted to further process SOM outputs and acquire the optimal clustering scheme. Finally, groundwater samples are categorized based on the minimum Davies-Bouldin Index (DBI)[73].

Cluster analysis represents a fundamental unsupervised learning algorithm in machine learning[74]. Of all available algorithms, K-means clustering enjoys widespread popularity due to its simplicity and computational efficiency[75]. As a widely adopted dimensionality reduction technique, PCA can project the original high-dimensional variables onto fewer new orthogonal principal components to achieve data dimension reduction[76]. It is a commonly used analytical method in hydrochemistry. While simplifying data complexity, it retains key information for understanding underlying relationships. However, PCA is highly sensitive to extreme values[77].

In this study, SOM, K-means clustering, and PCA were calculated using MATLAB R2025b, and PCA was validated using IBM SPSS Statistics 23. To avoid the impact of unit discrepancies, all data were converted to mg/L first and then normalized to Z-scores. For elements in partial samples with concentrations beneath the detection limit, the values were set to half of the detection limit, which is a commonly used method in environmental monitoring[78].

Water quality and health risk assessment

WQI

WQI is a dimensionless environmental index capable of comprehensively characterizing overall water quality status[79]. It is also regarded as one of the oldest, unique and effectively applied tools for evaluating water quality. Horton of the United States proposed the concept of a water quality index[80], who developed a scale for these parameters, ranging from 0 to 100 for different quality conditions, with 0 being the worst water quality and 100 being the best water quality, with the exception of temperature and obvious sensory contamination[81].

The calculation of WQI in this study consists of four steps. First, each chemical parameter was assigned a weight between 1 and 5, where 1 indicates the least impact on water quality and 5 indicates the most significant impact. The relative weight of each parameter was then obtained by dividing its assigned weight by the sum of all weights. Subsequently, the quality score of each indicator was calculated as the ratio of the measured concentration in each sample to the corresponding WHO drinking water guideline value, followed by multiplication by 100. Finally, the sub-index for each parameter was determined by multiplying its relative weight by its quality rating, and the WQI value for each sample was obtained by summing all sub-indexes[82–84]. After calculation, the calculated WQI should be classified according to the standard put forward by by Sener et al[85]. It was divided into five hierarchical levels, including excellent, good, poor, very poor, and unfit for drinking, with corresponding threshold limits of $WQI \leq 50$, $50 < WQI \leq 100$, $100 < WQI \leq 200$, $200 < WQI \leq 300$, and $WQI > 300$, respectively.

HHRA

As an effective evaluation tool developed by the U.S. Environmental Protection Agency (USEPA), HHRA aims to quantify adverse health outcomes and the exposure probability of humans to chemical contaminants in contaminated settings[86]. Four major components are included in this assessment framework: hazard recognition, dose-response analysis, exposure assessment, and risk quantification. Based on the HHRA, water quality impacts on human health fall into two categories: children and adults. The health evaluation criteria are based on the hazard index (HI) values. Exposure measures for direct ingestion (ADDingestion) and skin absorption (ADDdermal) are calculated by the following formula[38].

$$ADD_{ing}=\frac{C_W \times IR \times EF \times ED}{BW \times AT}$$

$$ADD_{der}=\frac{C_W \times SA \times K_P \times ET \times EF \times ED \times 10^{-3}}{BW \times AT}$$

Where,

Cw - actual concentration of the water quality parameters in the water (mg/L);
EF - exposure frequency (day/year);
AT - average time (days);
IR - ingestion rate (L/day);
ED - exposure duration in years (year);
K_p - coefficient of each elements for dermal activity (cm/h^{-1});
SA - average surface area of the skin exposed to each elements (cm^2);
ET - the exposure time (h/day);
BW - average body weight (kg).

In addition, the US Environmental Protection Agency (USEPA) has proposed a method for estimating the potential health risks related to non-carcinogenic metal exposure. The calculation procedure is as follows.

$$HQ_{ing}=\frac{ADD_{ing}}{RfD}$$

$$HQ_{der}=\frac{ADD_{der}}{RfD}$$

$$HI=\sum\left(HQ_{ing}+HQ_{der}\right)$$

Where,

HQ_{ing} and HQ_{der} - Hazard Quotient of ingestion and dermal

Generally speaking, larger HI or HQ belongs to higher health risk. If the calculated HI index is >1, it means the health risk was considered unacceptable[87]. On the contrary, HI value less than 1 means that the exposed person will not experience obvious adverse health effects.

Results and Discussion

Identification and characterization of hydrochemical clusters

Table S1 presents a comprehensive statistical summary of the hydrochemical parameters for all water samples. The temperature of the samples ranges from 18.9 ℃ to 98.7 ℃, with a mean of 39.04 ℃. Total dissolved solids (TDS) show wide variations, with values spanning ranging from 61.22 mg/L and 29960.18 mg/L, averaging 1306.31 mg/L. Groundwater pH ranges from 5.9 to 12.83 and averages 7.95, indicating an overall neutral to weakly alkaline environment. Major cations display mean concentrations in the order: Na^{+}> Ca^{2+}> K^{+}> Mg^{2+}> Li^{+}, while the major anions exhibit an average concentration sequence of Cl^{-}> HCO_3^{-}> SO_4^{2-}> F^{-}> CO_3^{2-}> Br^{-}> NO_3^{-}.

A total of 11 parameters were utilized for SOM-KM analysis. The selection of these parameters was based on previous dimensionality reduction results. Both the quantization error (QE) and topographic error (TE) were calculated for SOM of varying dimensions. To select an optimal map size and minimize the number of empty neurons, it was necessary to ensure the minimization of both QE and TE. After multiple configuration tests, the number of empty neurons reached the minimum when QE is 0.99 and TE is 0.016. At this point, a hexagonal grid composed of 60 neurons(6×10)is identified as the optimal configuration[88]. On this basis, the SOM model was used to establish a self-organizing map (Fig.2a) consisting of 60 neurons arranged in a hexagonal grid. The optimal number of clusters was determined as five, based on the KM clustering algorithm and the DBI[73]. As shown in Fig.2b, the composition of neurons is represented using a color code, where red indicates high values and blue signifies low values. The color coherence among neurons reflects synergistic relationships between the parameters for each water sample. The color gradient across the entire hexagonal lattice provides a clear visualization of the inter-variable relationships. The five clusters identified by SOM-KM analysis exhibit distinct hydrochemical characteristics, which are further illustrated by their positions in the Piper diagram (Fig.3). Table 1 presents hydrochemical data of each cluster, including basic parameters and major ions.

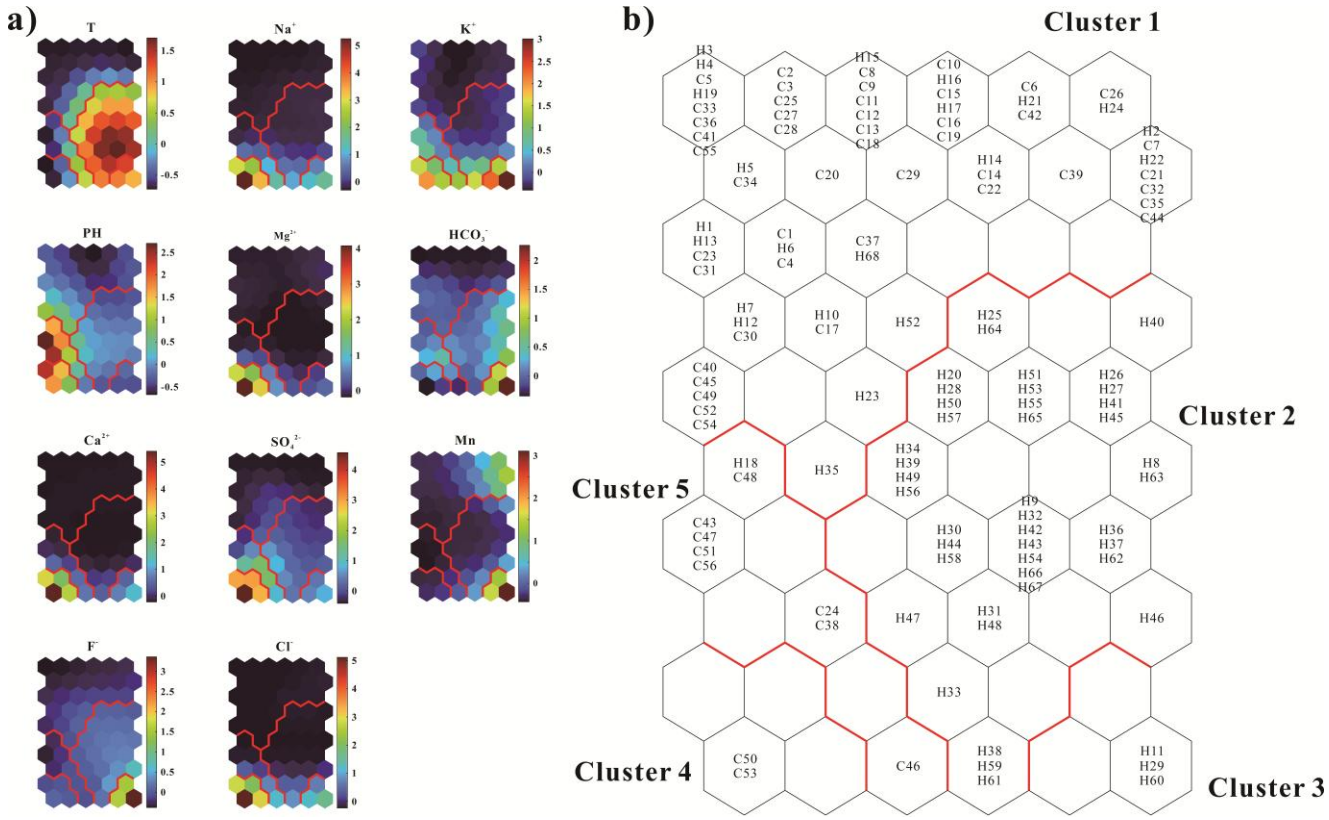


Figure 2. SOM analysis of groundwater hydrochemical characteristics. (a) SOM matrix map of hydrochemical parameter components. (b) SOM matrix map of groundwater sample clustering

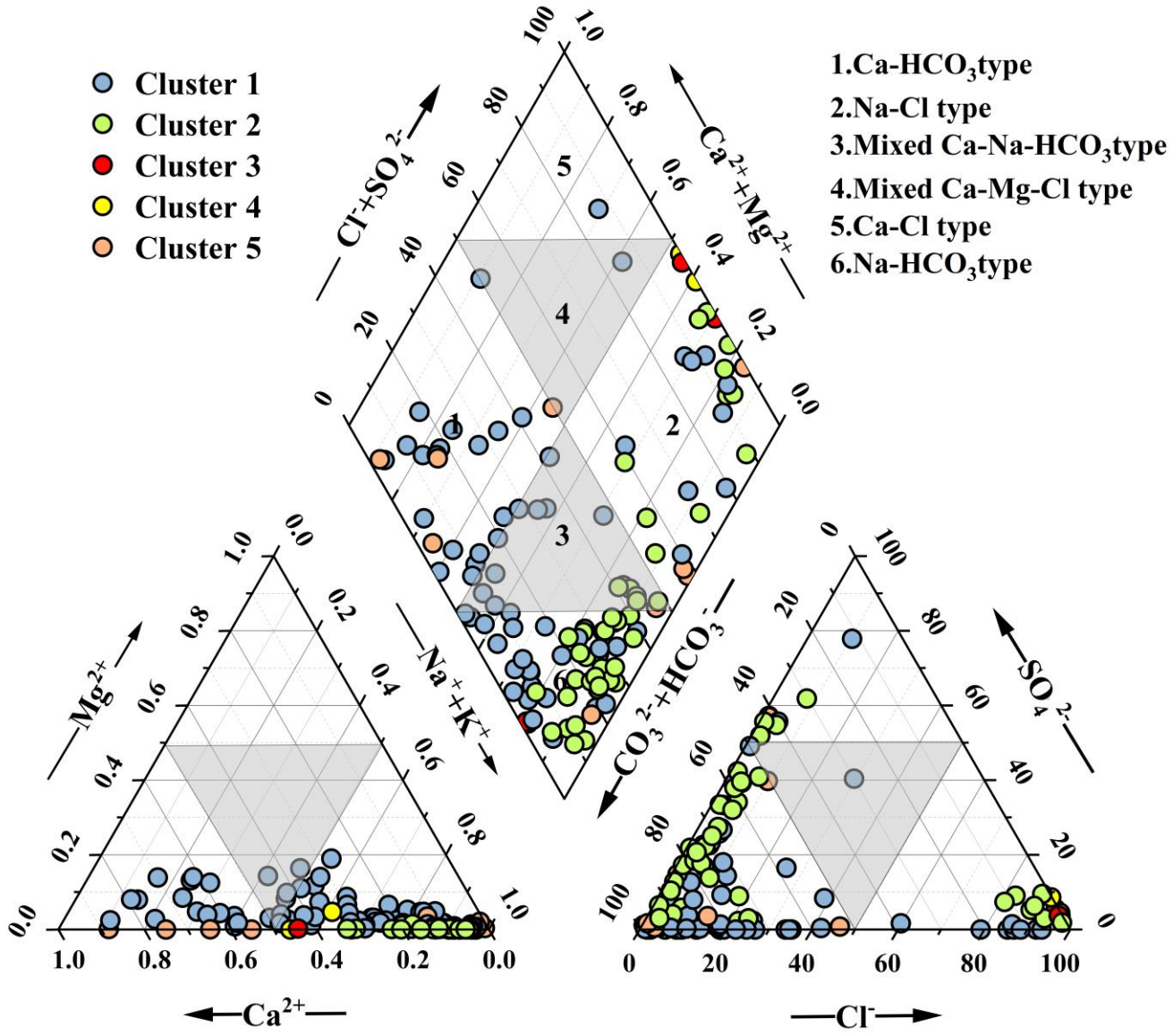


Figure 3. Piper trilinear diagram showing hydrochemical facies of groundwater samples grouped by five hydrochemical clusters

Cluster 1 comprises 68 samples, accounting for 54.8% of the total. Concentrations of Na^+, K^+, Mg^{2+}, Ca^{2+}, SO_4^{2-}, Cl^-, and F^- are relatively low, and the cluster is dominated by cold water. Hydrochemical types are diverse but share a common feature of high HCO_3^- concentrations, with the dominant types being Na-HCO_3, Ca-HCO_3 and Ca-Na-HCO_3. Cluster 2 contains 42 samples (33.9%). Concentrations of Na^+, Mg^{2+}, Ca^{2+}, and Cl^- are relatively low, and the cluster is dominated by hot water. All samples occur in the low-Ca and low-Mg zone, with main hydrochemical types including Na-Cl, Ca-Na-HCO_3, and Na-HCO_3. Cluster 3 includes only 3 samples (2.4%), characterized by distinctly high concentrations of K^+, HCO_3^-, Mn, and F^-. All samples are hot water, with a uniform Na-Cl hydrochemical type. Cluster 4 consists of 2 samples (1.6%), identified by high concentrations of Na^+, Mg^{2+}, Ca^{2+}, SO_4^{2-}, and Cl^-. All samples are cold water and classified as Na-Cl type. Cluster 5 comprises 9 samples (7.3%), mainly distributed at the interface between cold and hot water with high pH values. Hydrochemical types are variable, featured by high

concentrations of CO_3^{2-}+HCO_3^- and Na^++K^+, and low Mg^{2+}. The dominant water types are Ca-HCO_3 and Na-Cl. All results are presented in Fig.2 and Fig.3.

To further constrain the recharge sources and evolution pathways of the five hydrochemical clusters, stable isotope compositions ($\delta^{18}O$ and δD) were analyzed. $\delta^{18}O$ values are controlled by the isotopic signature of recharge water, meteorological conditions during recharge, and isotopic exchange and fractionation during water migration through the vadose zone and aquifer. In arid and semi-arid regions, strong evaporation prior to infiltration causes significant $\delta^{18}O$ enrichment in groundwater. Groundwater recharge sources can thus be effectively identified using isotopic compositions[86,89–92].

The $\delta^{18}O$ values of thermal water range from -8.70‰ to -5.26‰ with corresponding δD values spanning from -56.30‰ to -32.51‰, while the $\delta^{18}O$ values of cold water vary between -8.17‰ and -2.56‰ and δD values range from -52.26‰ to -18.19‰, With respect to the average $\delta^{18}O$ and δD values of the five clusters, they are -6.69‰ and -40.52‰ for Cluster 1, -6.70‰ and -47.31‰ for Cluster 2, -6.69‰ and -38.55‰ for Cluster 3, -4.99‰ and -19.65‰ for Cluster 4, -6.53‰ and -42.71‰ for Cluster 5, respectively (Table 1).

Most water samples lie near the global and local meteoric water lines (Fig.4), revealing precipitation as the dominant recharge source for regional groundwater. Cluster 1 dominated by cold water represents such a source and can be taken as the background. Cluster 2, which is dominated by hot water, shows more negative δD and $\delta^{18}O$ values than Clusters 1, 4, and 5, which are dominated by cold water, indicating that geothermal fluids are recharged by precipitation from higher mountainous areas with longer circulation paths and deeper circulation depths. Evaporation is not the dominant process[93]. Combined with the low calcium and magnesium concentrations and high-temperature conditions observed in the Piper diagram, these samples suggest long-term high-temperature water-rock interactions. Although Cluster 3 consists of hot water samples, it plots with the cold water cluster in the diagram. This discrepancy may result from rapid mixing with shallow groundwater or insufficient time for isotopic equilibration during rapid ascent. Cluster 4 shows simultaneous enrichment of hydrogen and oxygen isotopes and shifts toward the upper right of the diagram. Combined with the inset in the lower right corner, it can be inferred that it may be influenced by seawater mixing or evaporative fractionation. Cluster 5 displays intermediate isotopic values and plots along the LMWL, suggesting a transitional zone where different water sources mix.

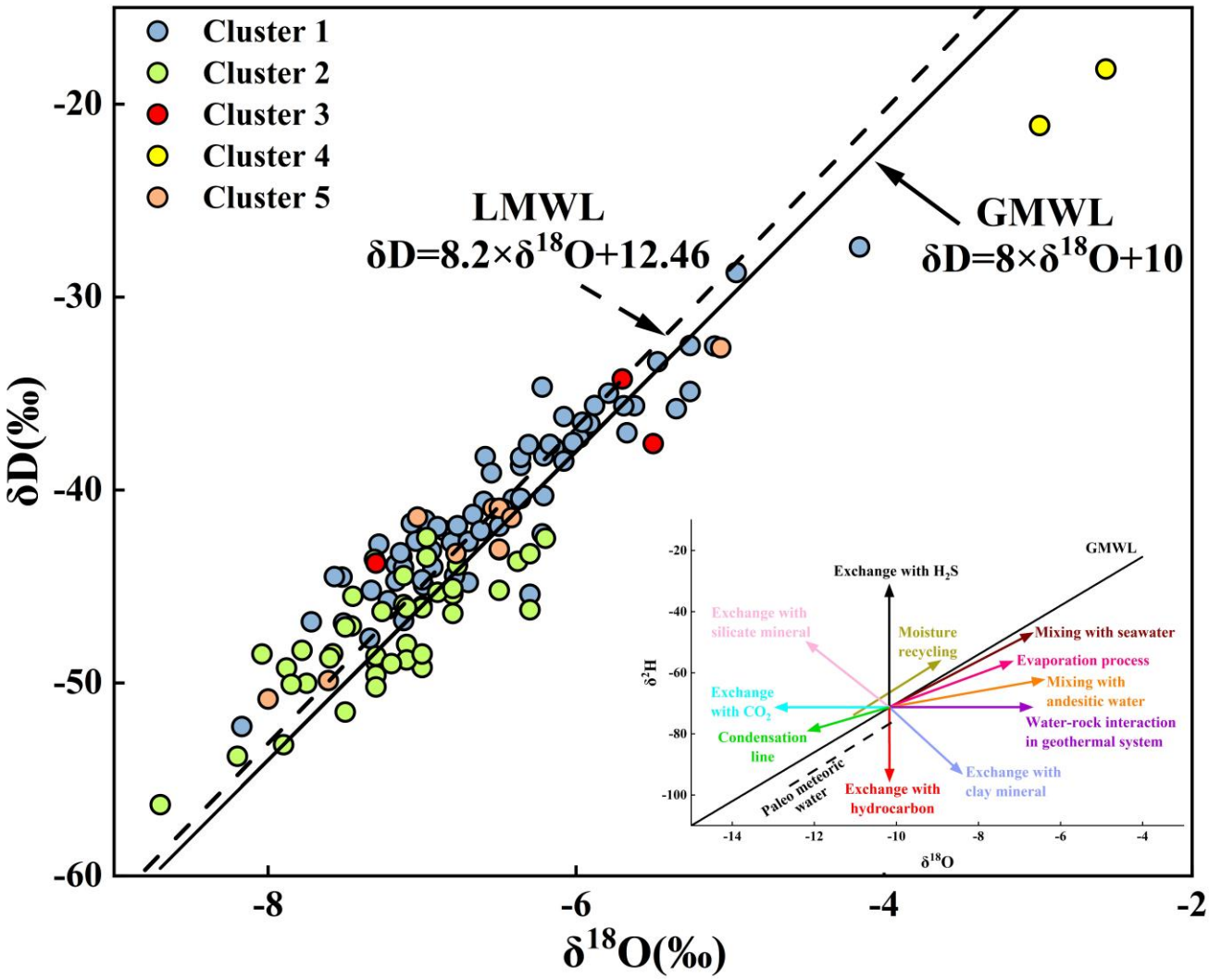


Figure 4. Relationship between $\delta^{18}O$ and δD of groundwater classified into seven categories. Isotopic trend curves revealing hydrologic processes and water-rock interaction behaviors were referenced from Pang et al[94]. LMWL comes from Jie et al[95].

Table 1. Major ion concentrations and isotopic compositions ($\delta^{18}O$, δD) of water samples in each cluster.

319

		T (°C)	pH	conductivity µS/cm	Li^+ mg/L	Na^+ mg/L	K^+ mg/L	Mg^{2+} mg/L	Ca^{2+} mg/L	F^- mg/L
Cluster 1	Average	24.84	7.69	392.93	0.08	54.64	4.91	3.85	25.27	3.94
	Min	19.00	6.88	35.44	0.00	1.20	0.41	0.00	3.73	0.56
	Max	48.20	8.92	1573.00	0.42	260.88	19.45	19.99	125.37	16.71
Cluster 2	Average	65.21	7.80	1331.63	0.40	243.77	10.09	0.92	58.58	10.92
	Min	45.00	5.90	185.40	0.09	74.09	2.08	0.00	2.89	2.45
	Max	98.70	8.48	7730.00	1.58	1296.17	67.40	4.61	548.95	23.61
Cluster 3	Average	53.43	7.56	13406.33	2.71	2053.92	76.96	34.51	1113.36	83.58
	Min	25.00	7.21	2929.00	1.36	761.08	37.02	10.30	154.82	9.87
	Max	69.60	7.81	19140.00	3.88	3080.68	114.05	58.51	1913.00	180.40
Cluster 4	Average	23.00	9.80	43755.00	0.33	6311.04	56.03	251.98	4472.39	11.12
	Min	22.80	7.78	42400.00	0.00	6109.80	31.45	1.06	3645.79	11.07
	Max	23.20	11.82	45110.00	0.66	6512.28	80.62	502.91	5298.99	11.17
Cluster 5	Average	23.02	10.40	3434.81	0.59	499.09	21.64	15.26	132.53	3.98
	Min	18.90	7.61	307.00	0.02	10.55	3.12	0.00	2.72	0.57
	Max	25.30	12.83	15160.00	2.11	2889.44	107.25	121.23	490.02	13.73

		Cl^- mg/L	Br^- mg/L	SO_4^{2-} mg/L	NO_3^- mg/L	CO_3^{2-} mg/L	HCO_3^- mg/L	TDS mg/L	δ^{18}OVSMOW (‰)	δDVSMOW (‰)
Cluster 1	Average	58.81	0.29	21.13	2.56	0.31	120.66	293.94	-6.50	-40.52
	Min	1.06	0.00	0.00	0.00	0.00	20.18	61.22	-8.17	-52.26
	Max	514.53	5.09	241.88	58.73	21.09	367.09	870.78	-4.16	-27.41
Cluster 2	Average	302.19	2.80	92.67	1.60	11.74	212.74	882.44	-7.21	-47.31
	Min	3.23	0.00	8.02	0.00	0.00	29.01	186.30	-8.70	-56.30
	Max	3342.67	19.92	418.93	14.26	59.68	587.85	5171.60	-6.20	-42.46
Cluster 3	Average	5607.76	19.06	277.23	17.65	0.00	886.78	10164.21	-6.16	-38.55
	Min	8.27	0.00	30.24	0.00	0.00	54.24	3562.88	-7.30	-43.79
	Max	9405.20	38.12	433.01	47.35	0.00	2522.96	14358.40	-5.50	-34.25
Cluster 4	Average	16586.05	182.63	1152.24	130.76	0.00	27.12	29181.70	-2.77	-19.65
	Min	15873.70	173.61	813.68	130.08	0.00	22.71	28403.22	-2.99	-21.11
	Max	17298.40	191.66	1490.80	131.45	0.00	31.54	29960.18	-2.56	-18.19
Cluster 5	Average	604.82	7.25	226.20	8.45	40.39	225.95	1786.14	-6.72	-42.71
	Min	1.42	0.00	1.09	0.53	0.00	5.05	182.87	-8.00	-50.83
	Max	5289.29	64.95	999.32	52.74	91.82	632.00	9113.02	-5.06	-32.63

Geochemical processes controlling hydrochemical differentiation

Ion ratios and composite ion ratios are of great significance in hydrochemical investigations of geothermal systems, and facilitate the identification of water-rock interactions along subsurface fluid circulation pathways[96–98]. The ratio of cation concentration to chloride ion concentration is one of the core parameters for characterizing the ionic composition characteristics, genesis, and evolutionary processes of aqueous systems[99].

As shown in Fig.5a, all data points plot approximately along a line with a slope of -1, indicating that cation exchange is the dominant process[100]. The majority of points (belonging to Clusters 1, 2 and 5) are distributed near the origin, suggesting weak ionic exchange. Their hydrochemical characteristics are primarily controlled by rock weathering and atmospheric precipitation. Clusters 3 and 4 are located in the second quadrant, indicating the release of Ca^{2+}, where Na^{+} in the aquifer has exchanged with Ca^{2+} and Mg^{2+} from the host rock. In contrast, a small number of points in Cluster 5 displays an opposite trend, which may be attributed to the minor release of Na^{+}, indicating the reverse cation exchange process with limited sodium release.

In the Na-Cl diagram (Fig.5b), most points (Cluster 1 and 2) are distributed along the 1:1 line, representative of salt rock dissolution (Eq.(1)), which is consistent with the conclusion drawn from Fig.5a. Cluster 5 plots above the 1:1 line, likely due to silicate weathering or cation exchange. Clusters 3 lies significantly below the line, which is associated with evaporative concentration, evaporite dissolution, or anthropogenic impacts[101]. Cluster 4 shows extremely high Cl^{-} concentrations, indicating seawater intrusion. Fig.5c also uses the 1:1 line as the divider. Above this line, Cluster 2 is dominant, and SO_4^{2-} concentrations increase with increasing Ca^{2+}, suggesting gypsum dissolution (Eq.(2)). Meanwhile, Cluster 1 has moderate calcium ion concentrations along with low sulfate concentrations, suggesting calcium ions are derived from carbonate weathering.

In addition, ion ratios including Ca/Na, Mg/Na and HCO_3^{-}/Na are commonly used to investigate the water-rock interactions between groundwater and different rock types[102]. Gaillardet et al[103] indicated that the Ca^{2+}/Na^{+}, Mg^{2+}/Na^{+} and HCO_3^{-}/Na^{+} ratios for the carbonate weathering endmember are approximately 50, 10 and 120, respectively, while those for the silicate weathering endmember are around 0.35±0.15, 0.24±0.12 and 2±1. Fig.5d presents the distribution of Ca/Na, Mg/Na and HCO_3^{-}/Na ratios of the collected water samples relative to three representative rock endmembers. As shown in Fig.5d, most samples (Cluster 1 and 2) are predominantly distributed near the silicate rock-dominated endmember, extending diagonally upward to the carbonate domain and downward to the evaporite domain, demonstrating that groundwater in this region is primarily controlled by the weathering and dissolution of silicate rocks. Cluster 3, Cluster 4 and a small portion of Cluster 2 extend downward to the boundary of evaporite rocks, indicating that part of the abnormal Cl^{-} concentrations in these clusters is derived from evaporite dissolution. Ca and Mg in groundwater are mainly derived from the weathering and dissolution of carbonate rocks and the dissolution of evaporites, whereas Na and K primarily originate from atmospheric precipitation, halite dissolution and silicate rock weathering. Combined with Fig.5(a-d), it can be concluded that the sources of Cluster 2 are highly diverse. Silicate weathering and cation exchange dominate, with minor contributions from gypsum dissolution. The sources of Cluster 1 are relatively simple, mainly falling in the transition stage from carbonate rock weathering to silicate rock weathering.

As shown in Fig.6, the groundwater sample points in the study area are roughly divided into three zones, with $[Ca+Mg+Na+K]/HCO_3=1$ and $[Ca+Mg]/HCO_3=1$ as the dividing lines.

Cluster 1 is mostly concentrated around [Ca+Mg+Na+K]/HCO_3=1, with a few ratios below 1. This distribution pattern indicates that these water samples are primarily controlled by silicate rock weathering, dominated by the dissolution of K-feldspar and Na-feldspar (Eq. (3) and (4)). Cluster 2 is located in the upper-left part of the inset plot and exhibits a steeper slope compared with Cluster 1. This may be attributed to the dissolution of halite which elevates Na^+ and K^+ concentrations, or evaporative concentration, which reduces the relative proportion of Ca^{2+} and Mg^{2+}. Combined with the low gypsum content in the hot water distribution area shown in Fig.1 and the evidence from Fig.5, it is inferred that these samples are derived from mixed sources, consistent with the conclusions demonstrated in Fig.5. Notably, Cluster 4 presents significant drift, which may indicate seawater intrusion, which requires further verification.

Fig.7 clarifies the formation mechanisms of each cluster. The Chloro-Alkali Indices (CAI_1 and CAI_2) can be used to analyze cation exchange and adsorption between groundwater and sediments (Eq. (5) and (6))[104].

As shown in Fig.7, groundwater samples in the study area can be divided into two groups based on the CAI: normal cation exchange and reverse cation exchange. Part of Clusters 1, 2, 3 and all of Cluster 4 are distributed in the first quadrant, showing characteristics of reverse cation exchange, with distinctly high CAI_2 values and CAI_1 close to zero. Given that parts of the study area are near the coast, two possible mechanisms account for this distribution. On the one hand, seawater intrusion causes an abnormal increase in Cl^- concentration in groundwater, which significantly amplifies the CAI_2 values. On the other hand, dissolved Na^+ and K^+ in groundwater may exchange with adsorbed Ca^{2+} and Mg^{2+} in the aquifer, leading to a decrease in aqueous Na^++K^+ concentrations(Eq. (7)). Combined with Fig.4, it can be concluded that the anomalous characteristics of Cluster 4 are mainly caused by the rapid salinity increase induced by seawater intrusion. Most samples from Clusters 1, 2, and 5 are concentrated in the third quadrant, showing typical normal cation exchange with significantly negative CAI_1 and CAI_2 close to zero. This indicates that Ca^{2+} and Mg^{2+} in groundwater displace adsorbed Na^+ and K^+ in silicate and carbonate media, which is the dominant water-rock interaction controlling the hydrochemical evolution of groundwater in the study area(Eq. (8)).

Based on the comprehensive analysis of ion ratios (Fig.5-7), five distinct hydrochemical evolution pathways have been identified. Cluster 1 represents shallow cold groundwater in the transitional stage from carbonate to silicate weathering, characterized by normal cation exchange (Eq. (8)) and feldspar dissolution (Eq. (3) and (4)). Cluster 2 exhibits the most complex sources, which dominated by silicate weathering and reverse cation exchange and minor contributions from gypsum and halite dissolution(Eq. (7)). Cluster 3 shares similar processes with Cluster 2 but with stronger reverse cation exchange and greater evaporite dissolution influence. Cluster 4 displays anomalous characteristics with extremely high Cl^- concentrations and elevated CAI_2 values, providing strong evidence for seawater intrusion. Cluster 5 represents a transitional water type with weak normal cation exchange and balanced carbonate-silicate weathering contributions. Overall, the spatial distribution of groundwater clusters reflects distinct hydrogeological settings: shallow meteoric recharge zones, deep geothermal circulation systems, coastal seawater intrusion zones, and transitional zones.

$$NaCl=Na^+ + Cl^- \quad (1)$$

$$CaSO_4 \cdot H_2O = Ca^{2+} + SO_4^{2-} + 2H_2O \quad (2)$$

$$2NaAlSi_3O_4 + 2H_2CO_3 + 9H_2O = Al_2Si_2O_5(OH)_4 + 2Na^+ + 4H_4SiO_4 + 2HCO_3^- \quad (3)$$

$$2KAlSi_3O_4+2H_2CO_3+9H_2O=Al_2Si_2O_5(OH)_4+2K^++4H_4SiO_4+2HCO_3^- \quad (4)$$

$$CAI_1=[Cl^--(Na^++K^+)]/Cl^- \quad (5)$$

$$CAI_2=[Cl^--(Na^++K^+)]/[SO_4^{2-}+HCO_3^-+CO_3^{2-}+NO_3^-] \quad (6)$$

$$2(Na^++K^+)^{2+}+(Ca,Mg)X_2=(Ca,Mg)^{2+}+2(Na,K)X \quad (7)$$

$$(Ca,Mg)^{2+}+2(Na,K)X=2(Na^++K^+)+(Ca,Mg)X_2 \quad (8)$$

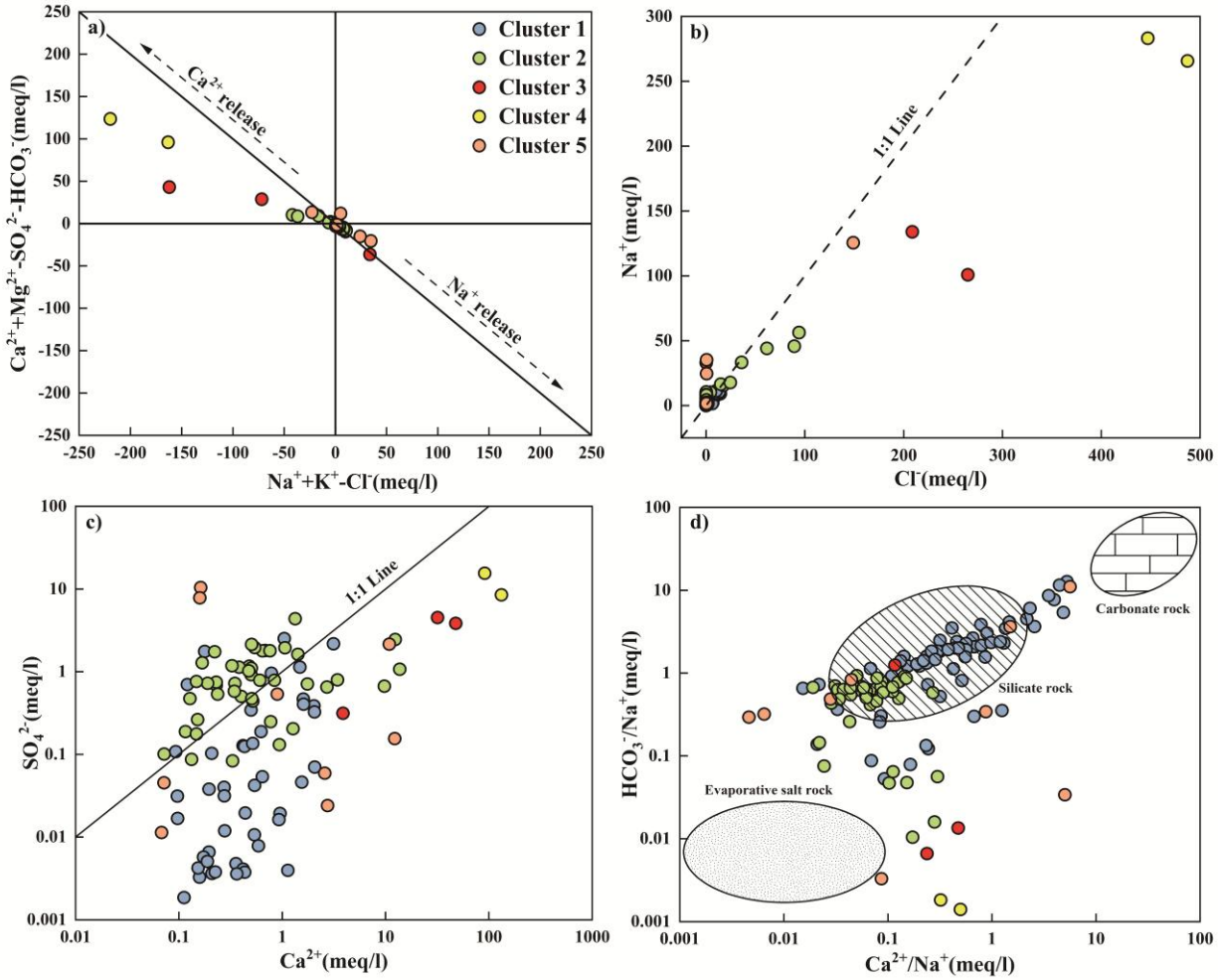


Figure 5. The ion ratio plot is presented above.(a)$(Ca^{2+}+Mg^{2+}-SO_4^{2-}-HCO_3^-)/(Na^++K^+-Cl^-)$;(b) Na^+/Cl^-;(c) SO_4^{2-}/Ca^{2+}; (d)$(HCO_3^-/Na^+)/(Ca^{2+}/Na^+)$

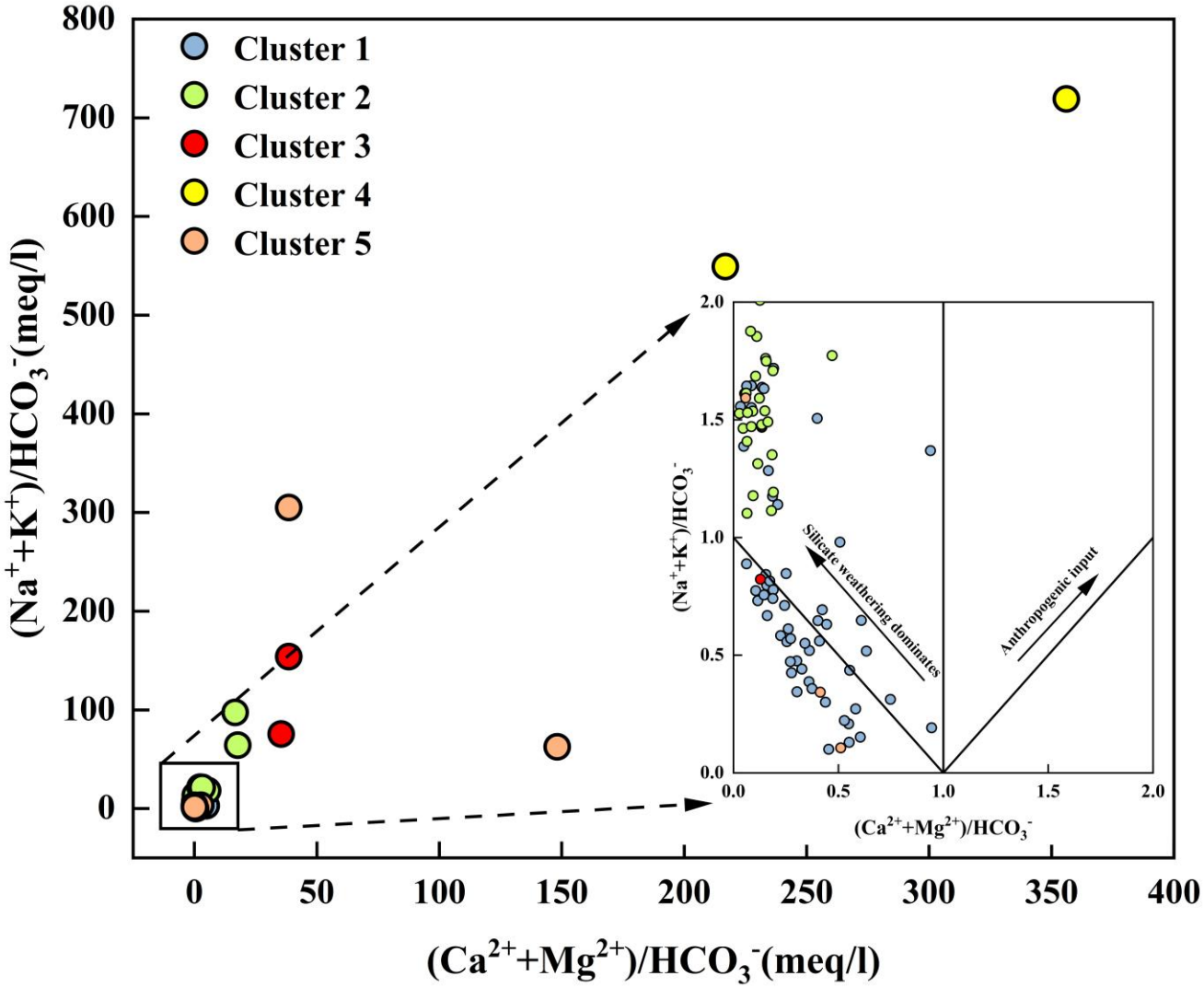


Figure 6. Plot of $(Ca^{2+}+Mg^{2+})/HCO_3^-$)/(($Na^+$+$K^+$)/$HCO_3^-$)

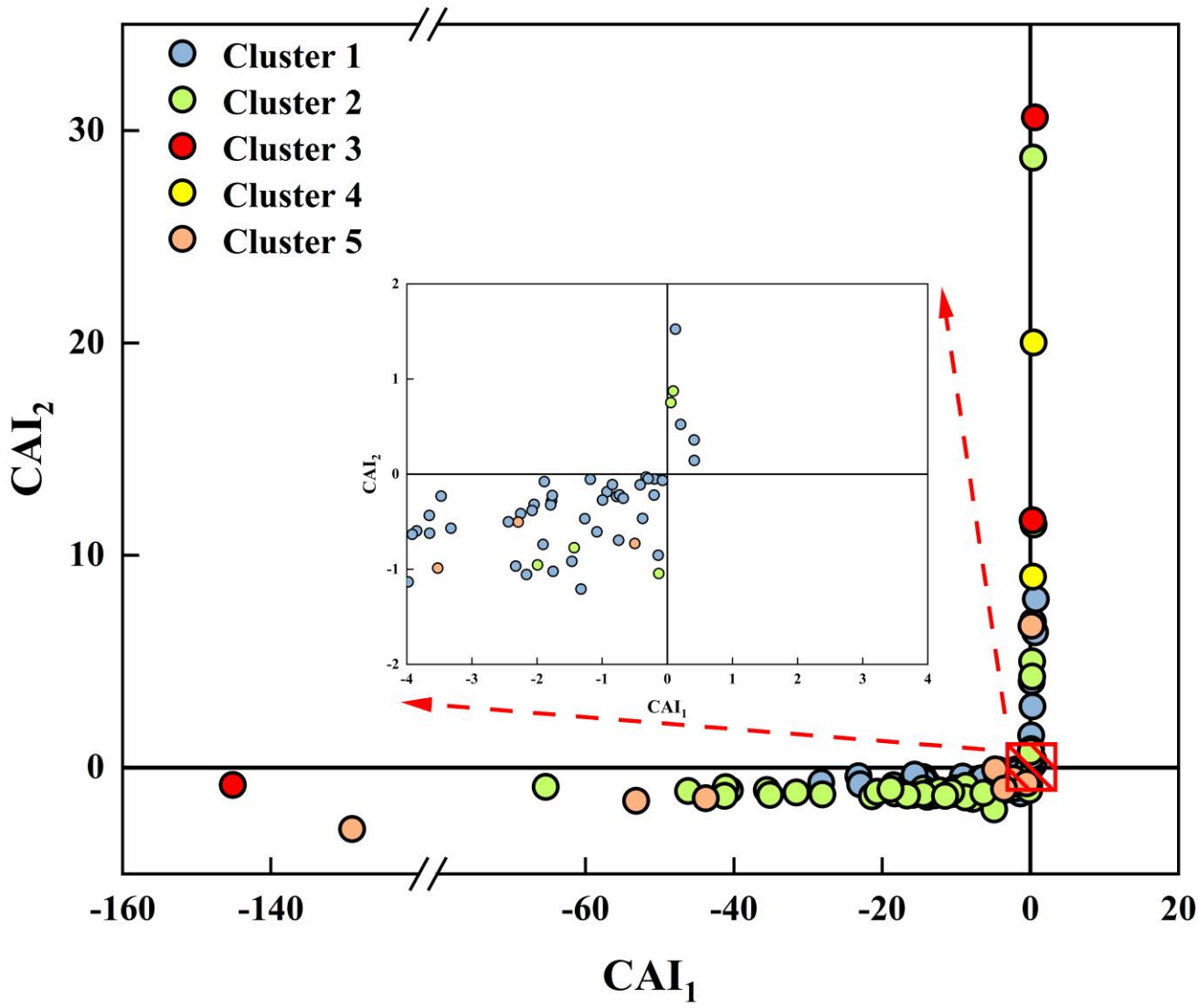


Figure 7. Diagram of CAI_1 vs.CAI_2

PCA: validation and integrated interpretation

Based on the hydrochemical characteristics revealed by ion correlation analysis, trace element analysis further elucidates the distinct water-rock interaction characteristics of each cluster. All trace elements were screened via dimensionality reduction analysis in SPSS, and subsequently selected As, Mn, B and Ba for subsequent SOM-KM analysis. In combination with the anionic-cationic exchange and K-feldspar/Na-feldspar dissolution processes discussed previously, major ions and trace elements were combined to carry out PCA. The variance explained by each principal component is summarized in Table 3. The first three principal components account for 59.9% of the total variance (Fig.8), and the four principal components explain 69.67% of the total variance, which captures the characteristics of geological processes to a certain extent. The outcomes satisfy the Bartlett sphericity test and significance test at $p < 0.001$ and $p < 0.05$ respectively, strongly validating the applicability and reliability of PCA. These results extend the previous hydrochemical interpretation by integrating major ion evolution, trace

element mobilization, water-rock interaction, and possible deep fluid influence into a unified analytical framework.

Table 2.Principal component loadings and variance contributions of hydrochemical variables

	PC1	PC2	PC3	PC4	PC5
T	0.039	0.163	-0.654	0.108	0.184
pH	0.102	-0.039	0.231	0.623	0.260
Na	0.446	-0.082	0.030	-0.065	0.046
K	0.320	0.173	-0.065	0.322	-0.293
Mg	0.308	-0.143	0.172	-0.366	0.246
Ca	0.420	-0.142	0.077	0.057	-0.098
F	0.202	0.182	-0.439	0.079	-0.398
Cl	0.440	-0.120	0.006	-0.011	-0.102
SO4	0.367	-0.105	-0.014	-0.146	0.314
HCO3	0.015	0.563	0.165	-0.151	0.281
As	-0.006	0.163	0.132	0.434	0.329
Mn	0.078	0.549	0.217	-0.287	-0.191
Ba	0.078	0.205	0.398	0.184	-0.388
B	0.185	0.386	-0.186	0.012	0.314
Eigenvalues	4.749	1.966	1.494	1.307	1.062
Variance (%)	33.919	14.046	10.671	9.335	7.583
Percentage (%)	33.919	47.965	58.636	67.972	75.555

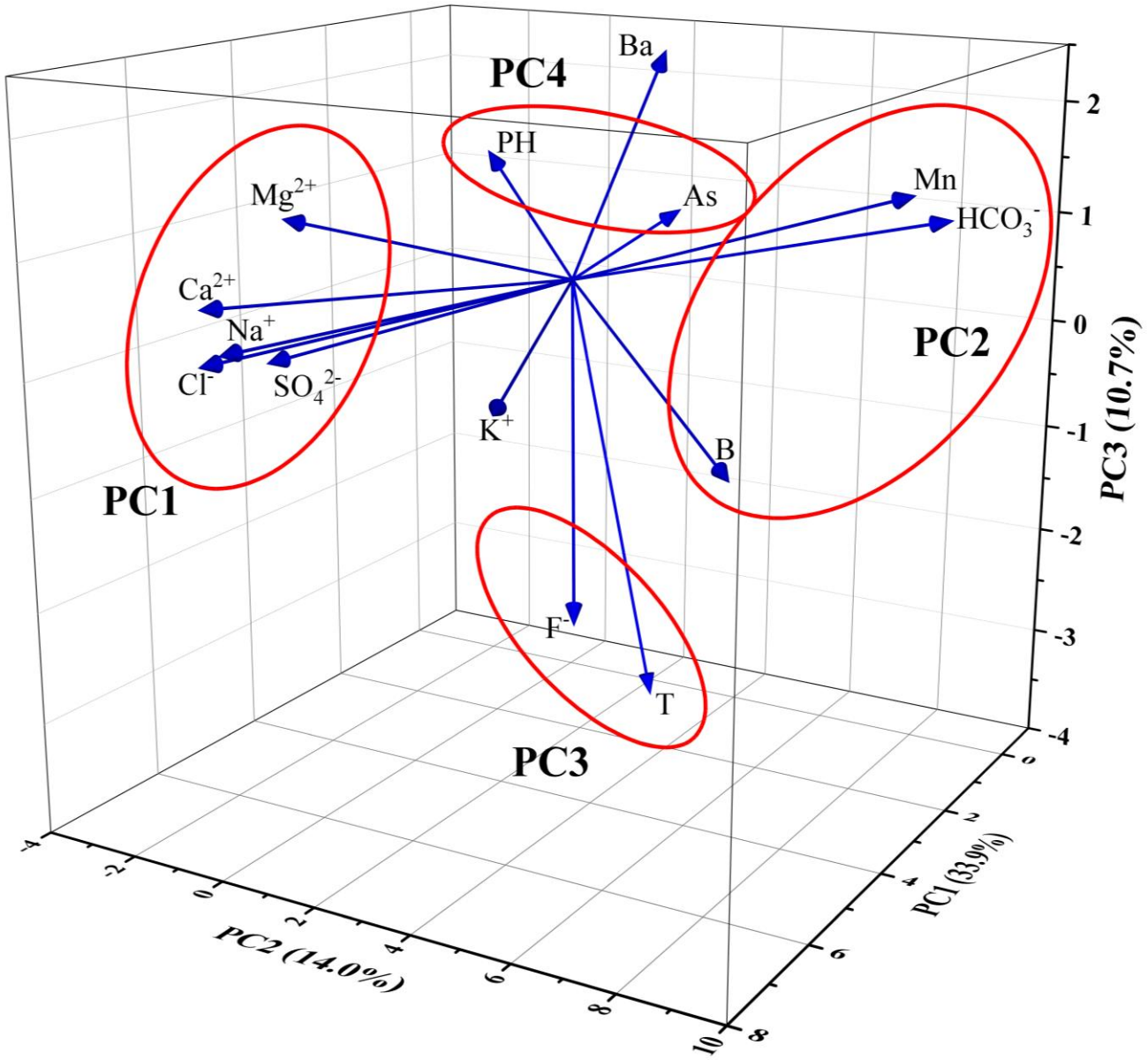


Figure 8. 3D loading plot of the PCA for groundwater hydrochemical parameters.

Among the influencing factors, Ca^{2+}, Mg^{2+}, Na^{+}, Cl^{-} and SO_4^{2-} dominate PC1 (33.9%). These ions extend along the positive direction of PC1 with the highest contributions. Strong correlations suggest that their concentrations are controlled by the same geological processes. The presence of Na^{+} and Cl^{-} indicates halite dissolution, while the occurrence of SO_4^{2-} represents the dissolution of gypsum and anhydrite. Ca^{2+} and Mg^{2+} are indicative of carbonate dissolution. Meanwhile, Cluster 4 shows the highest contribution to PC1, followed by Cluster 3 (Fig.9). As discussed above, Cluster 3 groundwater is significantly affected by evaporative concentration and accompanied by reverse cation exchange, while Cluster 4 is dominated by seawater intrusion. Although the two groups have distinct hydrogeochemical origins, they produce similar hydrochemical manifestations: a remarkable increase in major ion concentrations in groundwater. This outcome further validates the rationality of the above analysis. PC1 mainly reflects the natural salinity gradient associated with water-rock interaction and evaporite/carbonate dissolution. No

strong evidence from PCA alone indicates a dominant anthropogenic contribution to this component. Mn, B, and HCO_3^- dominate PC2 (14.0%), dominated by Cluster 3 (Fig.9). These ions extend along the positive direction of PC2, which is nearly perpendicular to PC1. The enrichment of HCO_3^- is directly related to the carbonic acid weathering of carbonate or silicate minerals. Manganese is commonly hosted in these minerals, so the two may be released simultaneously during mineral weathering. Under reducing conditions, Mn can stably exist in groundwater in the form of bicarbonate[105–107]. However, the correlation coefficient between Mn and HCO_3^- in Fig.10 is only -0.089, indicating no significant linear relationship between them. Combined with the PCA results, a preliminary conclusion can be drawn: the common source of HCO_3^- and Mn only reflects a similar environmental background rather than a direct linear correlation. The stable occurrence of Mn depends on the neutral to weakly alkaline environment provided by HCO_3^-. The weak correlation between Mn and major ions also supports this interpretation. B shows a moderate loading in PC2 (0.386), indicating that it is affected by a similar hydrochemical environment but has a relatively independent source, which may be related to the release from sediments or boron-bearing minerals. The dissolution of K-Na feldspar releases abundant HCO_3^-. Meanwhile, owing to the isomorphic substitution of boron, B may be released from boron-bearing silicate minerals, clay minerals, or sediments during water-rock interaction. The positive correlations of B with Na^+, K^+ and HCO_3^- shown in Fig.10 confirm the source of B.

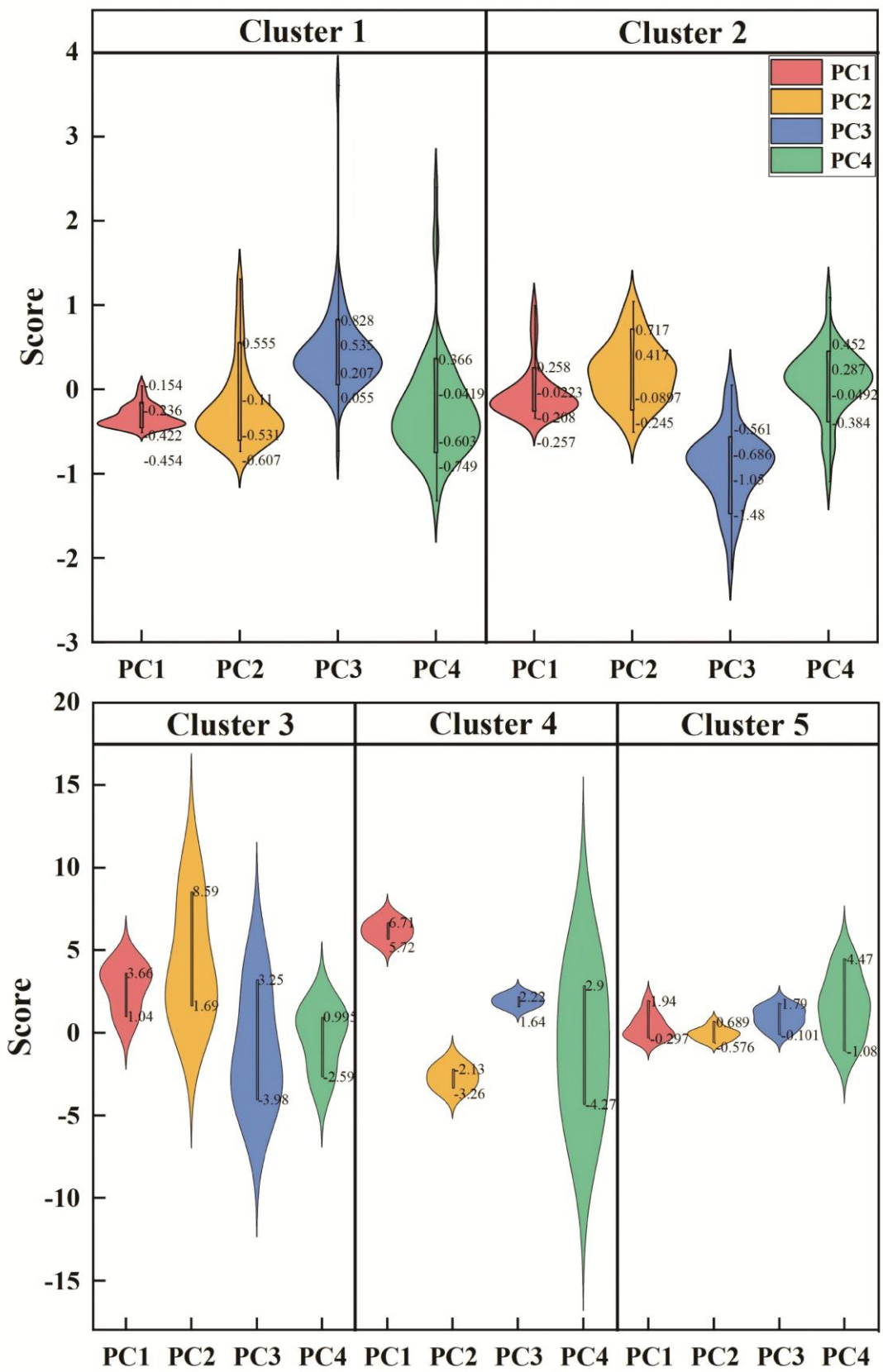


Figure 9. Violin plot of principal component (PC1-PC4) scores for five hydrochemical clusters

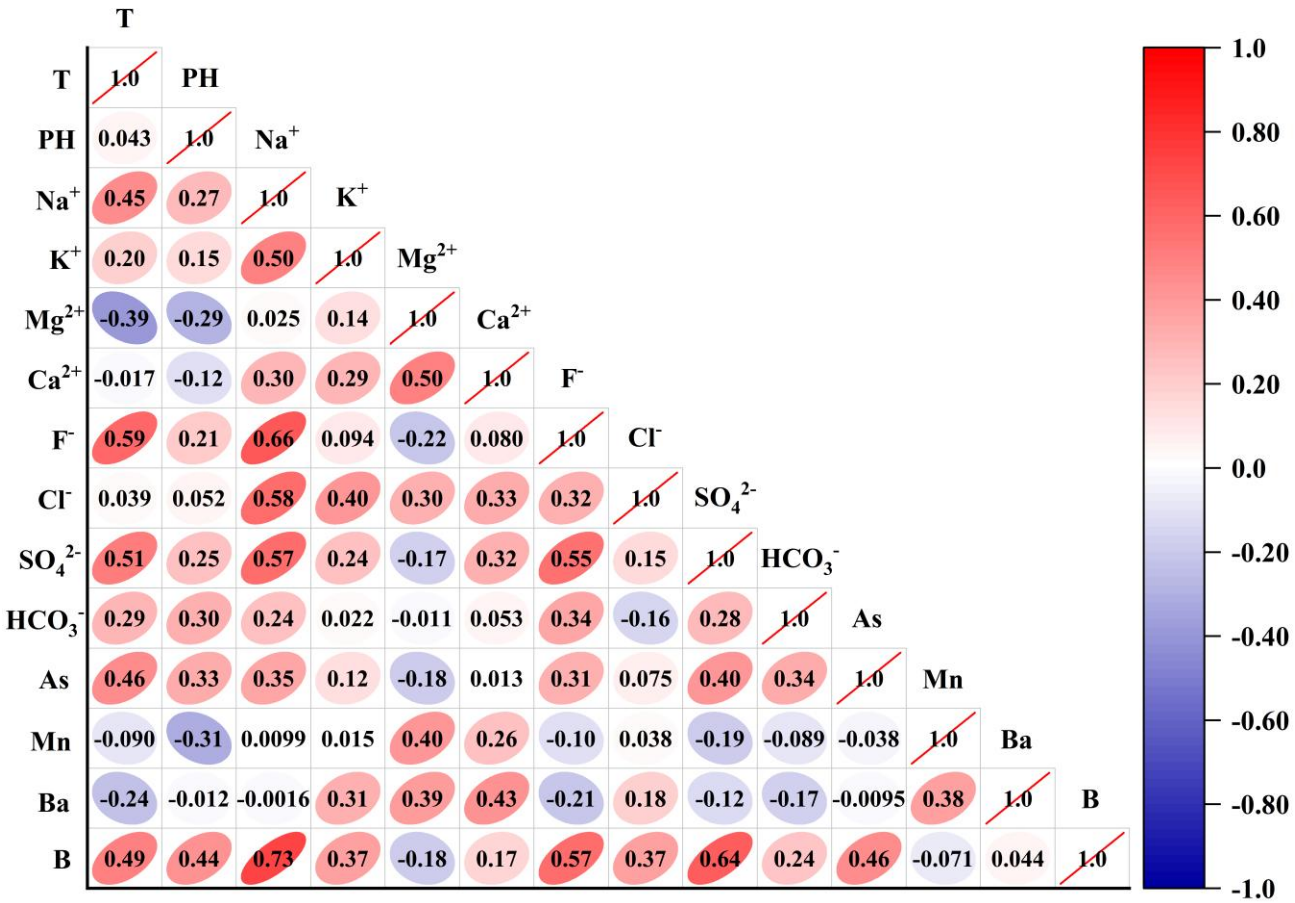


Figure 10. Spearman correlation coefficient diagram of major elements

Fig.11 shows the cross plot of Cl^- with B, in which five straight lines are presented. Different Cl/B ratios represent distinct sources of the water samples. Most samples are distributed near the lines for felsic minerals and local precipitation, and are mainly composed of Clusters 1, 2 and 5. Two samples from Cluster 3 and all samples from Cluster 4 are located above the seawater line, indicating seawater mixing in these samples, which has the same origin as Cluster 4 discussed above. The other samples above the seawater line are featured by extremely low B concentrations, excessively high Cl^- concentrations and a proportional increase in Na^+ concentrations, and thus the anomaly can be ascribed to halite dissolution.

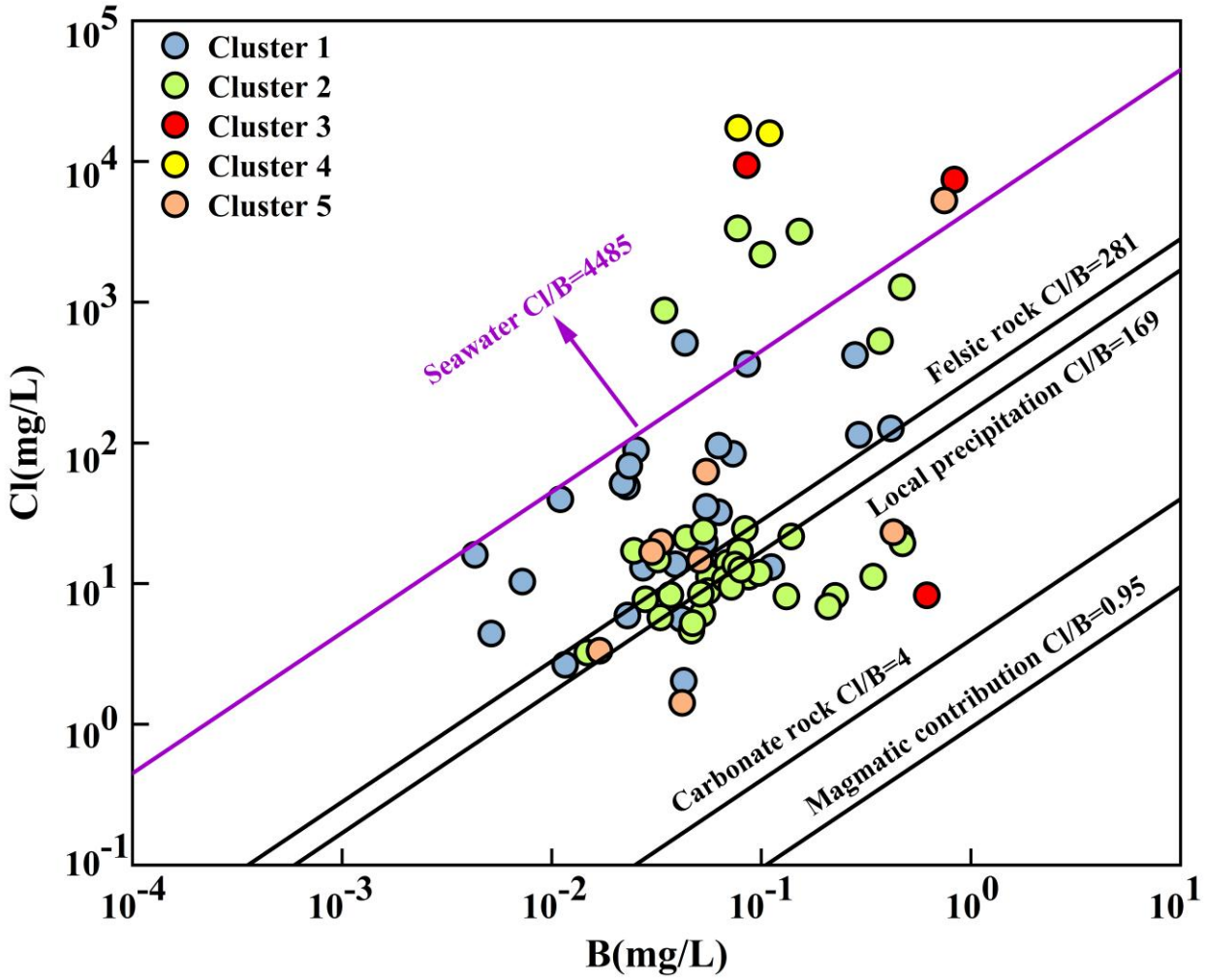


Figure 11. Relationship between Cl and B concentrations in groundwater with typical source end-member indicators

F^- and T constitute PC3 (10.7%), with these ions extending along the negative direction of PC3. Fluorine is abundant in granite, hydrothermal ore deposits and alkaline granite[108,109]. The maximum concentration of F^- in groundwater is generally controlled by the solubility of fluorite[110]. Other processes include Na-Ca cation exchange under specific conditions, which promotes the dissolution of CaF_2[111–113]. Fluorite is widely distributed in South China[114]. Groundwater continuously dissolves fluorite, releasing fluoride and calcium ions. The calcium ions in turn participate in cation exchange and are replaced by sodium ions, which promotes the dissolution reaction. The positive correlation between F^- and Na^+ in Fig.10 is consistent with this process. Fig.10 also shows that the correlation coefficient between Na^+ and Cl^- is 0.58, which is lower than the 0.66 between Na^+ and F^-, further supporting the rationality of this interpretation. Dissolution of fluoride-bearing minerals accelerates in high-temperature zones, which is further validated by the strong positive correlation coefficient of 0.59 between temperature and F^- shown in Fig.10[115].

As and pH jointly constitute PC4 (9.3%), which is dominated by Cluster 5. Numerous previous studies have demonstrated that microbially mediated reductive dissolution of ferric iron oxides and hydroxides occurs simultaneously with the oxidation of organic matter, releasing co-

precipitated arsenic previously adsorbed onto these minerals[116]. Thus, high arsenic concentrations commonly occur synergistically within reducing environments[117]. However, according to the statistical results, no significant positive correlation was observed between As and Fe, while As showed a weak positive correlation with pH (Fig.10). Accordingly, the potential geochemical process is proposed as follows: under reducing conditions, Fe(III) oxyhydroxides may undergo reductive dissolution, releasing adsorbed or co-precipitated As. The released Fe^{2+} may subsequently precipitate as siderite under carbonate-rich conditions, which could partly explain the weak As-Fe correlation. Meanwhile, arsenate and arsenite exist as oxygen-containing anions in groundwater. The increase in pH weakens mineral surface adsorption capacity, thereby promoting the release and enrichment of arsenic in aqueous solution.

In summary, multivariate statistical analysis further supplements and clarifies the natural hydrochemical evolution characteristics of the study area, while identifying anomalous elements in groundwater, providing a key basis for the assessment of regional hydrogeochemical evolution and environmental risks.

Integrated Assessment of Groundwater Quality and Health Risk

Drinking water quality assessment based on WQI

Building on the hydrochemical classification, ion correlation analysis and PCA results discussed above, this section further evaluates how the identified hydrogeochemical processes influence trace-element enrichment and water quality in the thermal spring system. The previous results indicate that the different clusters represent distinct stages or end-members of groundwater evolution, including background water-rock interaction, evaporative concentration, ion exchange and so on. These processes provide the geochemical basis for interpreting the spatial and cluster-dependent variations in trace elements. During the upward migration of geothermal fluids, prolonged circulation, elevated temperature and intensive water-rock interaction can enhance the dissolution of aquifer minerals and sediments, thereby promoting the release of potentially hazardous elements into groundwater[118–122].

Therefore, trace-element anomalies in different clusters are not only indicators of hydrogeochemical evolution, but also key factors controlling water quality and environmental risk. To assess their environmental significance, water quality evaluation was conducted according to the WHO guidelines and the GB 5749-2022. Although thermal spring waters may not be directly used as drinking water, comparison with drinking-water standards provides a useful reference for identifying anomalous elements and potential health-related concerns. The standards specify threshold limits for 12 trace elements, including Al, As, Ba, Cd, Co, Cu, Cr, Mn, Ni, Fe, Pb and Zn. The average, maximum and minimum concentrations of trace elements in each cluster are presented in Table 3.

Table 3.The main parameters of the concentration of trace elements in each cluster water sample

		Al µg/L	As µg/L	Ba µg/L	Cd µg/L	Co µg/L	Cr µg/L	Cu µg/L	Fe µg/L	Mn µg/L	Ni µg/L	Pb µg/L	Zn µg/L
	Average	25.14	1.21	178.81	0.04	0.09	0.19	2.54	20.44	152.18	1.78	1.85	11.40
Cluster 1	Min	3.54	0.06	17.50	0.01	0.02	0.06	0.24	1.33	0.53	0.11	0.23	2.30
	Max	78.59	21.42	3282.16	0.31	0.95	2.87	89.25	413	1206.21	57.43	95.18	116.63
	Average	19.97	1.59	61.27	0.05	0.19	0.51	0.92	12.97	69.61	2.85	0.38	3.82
Cluster 2	Min	0.58	0.06	0.10	0.00	0.00	0.00	0.00	0.00	0.06	0.00	0.03	0.17
	Max	84.22	7.37	369.95	0.17	2.78	8.15	10.10	132.00	487.00	35.9	2.6	26.1
	Average	45.44	2.13	482.86	0.11	2.32	1.02	1.84	30.77	1354.06	34.09	1.22	4.09
Cluster 3	Min	28.1	0.13	324.00	0.03	0.1	0.12	0.15	0.00	658.00	0.11	0.36	1.95
	Max	75.52	4.59	783.68	0.17	6.35	2.71	4.96	79.30	2726.97	101.00	2.51	8.35
	Average	16.61	0.39	391.88	0.02	0.04	0.1	0.89	7.39	60.22	0.49	0.88	7.00
Cluster 4	Min	13.72	0.34	300.70	0.02	0.03	0.09	0.64	4.60	0.48	0.41	0.61	6.96
	Max	19.51	0.45	483.06	0.03	0.04	0.11	1.14	10.18	119.95	0.56	1.15	7.04
	Average	260.13	3.48	167.44	0.04	0.04	0.22	2.42	23.21	7.87	0.70	1.08	6.79
Cluster 5	Min	23.99	0.12	19.34	0.02	0.03	0.08	0.63	2.46	0.45	0.32	0.34	3.01
	Max	1547.36	21.76	655.15	0.06	0.09	0.93	8.99	131.11	62.50	2.37	2.89	15.87

The WQI classification reveals an uneven distribution across quality categories: 85.48% of samples fall into the Excellent range, 9.68% are rated as Good, 4.03% as Fair, none as Poor, and only 0.81% as Unsatisfactory. Overall, over 95% of groundwater samples are suitable for drinking and household purposes but roughly 4.84% of samples exceeded the threshold of 100 which making themselves unacceptable for use. Spatially, these problematic samples are predominantly found in Cluster 3, with a few scattered cases also appear in Clusters 1 and 5. The highest WQI value reached 370.68 at site H11 in Cluster 3, driven by extremely high Mn concentration (>2000 μg/L). The highest WQI value reached 370.68 at site H11 in Cluster 3, with Mn contributing 349.61 (94%) of the total WQI (Table S2), corresponding to an extremely high Mn concentration (>2000 μg/L). Fig.12 shows the spatial distribution of WQI values, with the highest WQI samples (red zones) located in the north-central and southeastern parts of the study area.

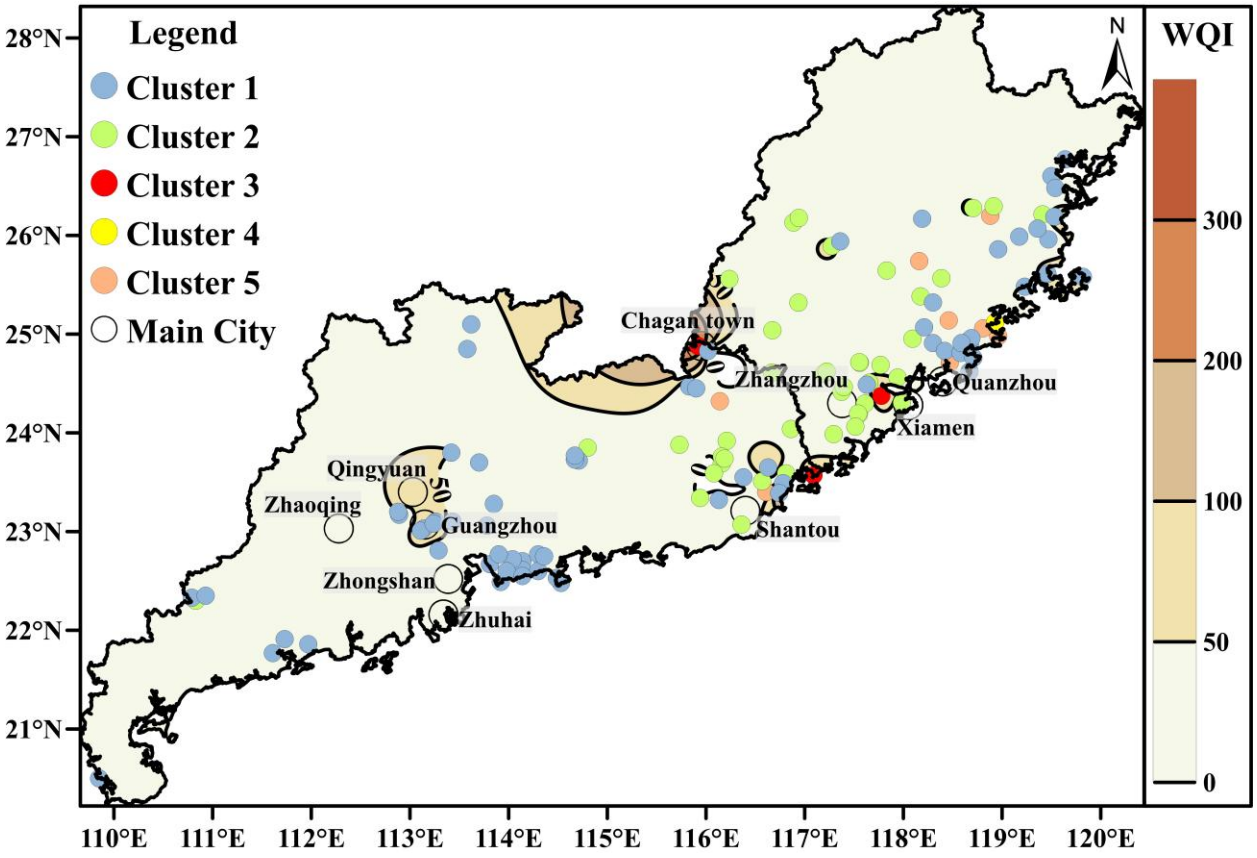


Figure 12. Overview of water quality evaluation in the study area

Exposure levels of elements vary markedly across different regions, with several areas exhibiting distinctly higher exposure values. According to the GB/T 14848-2017, the Class III toxicological limits for trace elements apply mainly to centralized drinking water sources as well as industrial and agricultural water uses. The limits are as follows: As(10 μg/L), Cd(5 μg/L), Pb(10 μg/L), Cr(50 μg/L), Al(200 μg/L), Fe(300 μg/L), Mn(100 μg/L), Cu(1000 μg/L), Zn(1000 μg/L), Co(50 μg/L), Ni(20 μg/L), Ba(700 μg/L). Based on the data in the Table S1, there are 3 outliers for As, 1 outlier for Pb, 2 outliers for Al, 1 outlier for Fe, 40 outliers for Mn, 6 outliers for Ba, 3 outliers for B and 4 outliers for Ni, while all other trace elements show no abnormal concentrations. Manganese ions show the highest number of abnormal values. Among the 40 Mn anomalies, 28 belong to Cluster 1, 8 to Cluster 2, 3 to Cluster 3, and 1 to Cluster 4. Among these trace elements,

manganese shows the most prominent pollution characteristics, with a total of 40 exceeding standard sites (accounting for 32.3% of all monitoring points), predominantly distributed in Cluster 1 (70%). The maximum manganese concentration reaches 2726 μg/L, 27 times the national standard limit. Mn possesses multiple valence states and readily undergoes redox transformation among different valence states under environmental influences[123]. Accordingly, manganese migration is sensitive under complex redox conditions.

The concentration distribution of manganese ions in groundwater is shown in Fig.13, with the concentration unit of Mn being μg/L. Thus, all values exceeding 100 μg/L in the figure are regarded as anomalies. Areas with excessively high manganese ion concentrations can be divided into four major distribution zones, dominated by the first two high-concentration anomaly regions. The first zone is the core ultra-high anomaly area in the north-central part, located at the junction of Guangdong, Jiangxi and Fujian provinces, where the central concentration exceeds 2000 μg/L. The second zone is the high-value anomaly area in the southeastern part, situated at the border of eastern Guangdong and southern Fujian, with a closed high-value center where the concentration is higher than 500 μg/L. Region 3 and Region 4 are located in the Zhangzhou-Quanzhou-Xiamen area and the Zhaoqing-Qingyuan-Guangzhou area, respectively, with both manganese concentrations ranging from 200 to 500 μg/L.

In Zone 1, the manganese anomalies are developed on the Silurian monzonitic granite and Upper Cretaceous strata. The granite itself contains Mn-rich minerals such as biotite, and the isomorphic substitution in K-Na feldspar significantly elevates Mn concentrations[124]. The Upper Cretaceous strata consist of purplish red siltstone, mudstone interbedded with glutenite, gypsum and mirabilite. The reducing environment reduces Mn^{4+} to divalent Mn^{2+}, which is released into groundwater[125]. Meanwhile, the evaporative concentration environment associated with gypsum and mirabilite further increases Mn concentrations. Additionally, slow groundwater runoff and limited external water exchange in this area collectively result in extremely high Mn anomalies. The synchronously high HCO_3^- concentrations suggest the formation of $MnHCO_3^+$ complexes[105], which also verify the geogenic source of Mn in this area.

In Zone 2, the Mn concentration anomalies are attributed to the reduction of Mn by abundant organic matter in Holocene strata, leading to Mn release into groundwater and pore water[126,127]. Another potential cause is the reduction of sulfate-rich seawater to produce H_2S. For Fe and Mn ions, the solubility of MnS is higher than that of FeS, making Mn more likely to remain dissolved in water[128,129]. The anomalous distributions in zone 3 and zone 4 are relatively scattered. These anomalies are relatively scattered and likely related to localized water-rock interaction and organic matter reduction. In contrast, low Mn areas (< 100 μg/L) are widely distributed in the Pearl River Delta (Guangzhou, Zhongshan, Zhuhai, Shenzhen) and western coastal regions (Zhanjiang), where rapid groundwater circulation and seawater dilution limit Mn^{2+} accumulation. High manganese levels in water can cause serious health problems. Excess manganese in drinking water can induce a range of neurological disorders and may even trigger cardiovascular toxic reactions in severe cases[130–132]. Thus, maintaining manganese ion concentrations within a stable range is therefore particularly essential.

Overall, high-manganese areas and high-WQI areas are highly overlapped in space. This confirms that Mn enrichment is the primary driver of water quality degradation in the study area. The overall water quality in the study area is relatively good, but attention is still needed in very few individual areas. The extreme point in Zone 1 is located near Chagan Town in Guangdong Province, through which the Nanyang River passes, serving as the main drinking water source for

local residents. Given that the abnormal manganese concentration is most likely derived from natural processes, and Guangdong has abundant rainfall, there is a possibility that leached water may enter the river. Therefore, it is recommended that the relevant local government regularly monitor the manganese concentration in groundwater, especially during the rainy season, so as to reduce the health risks caused by excessive manganese. The extreme point in Zone 2 is located in the urban area of Shantou, through which the Xinjin River flows into the sea. The abnormal concentration in this area is more likely attributed to seawater infiltration and organic matter reduction, showing no obvious seasonal characteristics. Thus, it is suggested that relevant personnel conduct regular and fixed-time water sampling and inspection to minimize the adverse effects of manganese on human health.

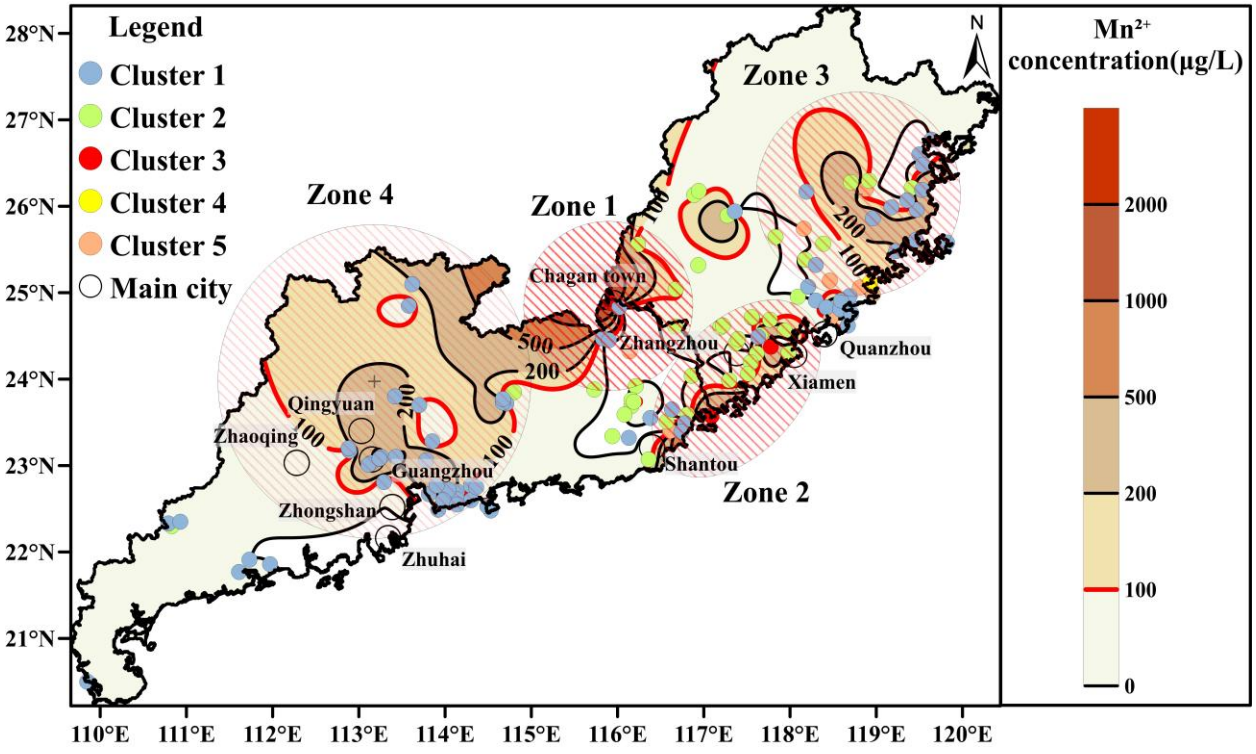


Figure 13. Groundwater manganese ion spatial distribution in the study area, with the red contour line at 100 μg/L representing the Class III limit (GB/T 14848-2017). Red hatched areas highlight four Mn anomaly zones.

HHRA: localized analysis based on hydrochemical clusters

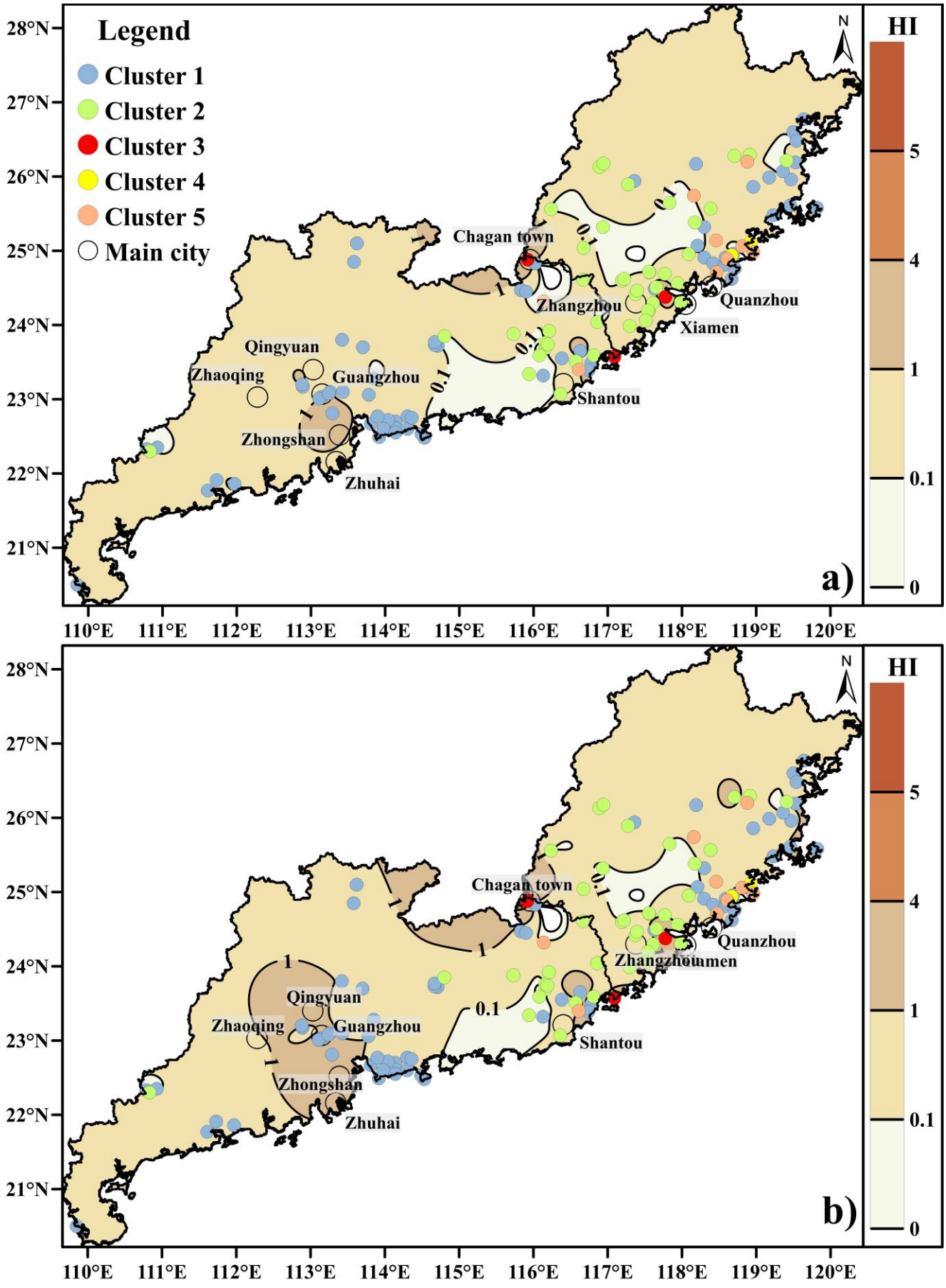
A HHRA model from the USEPA was employed to calculate the non-carcinogenic risks associated with daily groundwater use for adults and children. B ions were replaced by Co ions herein, since boron is mainly used for hydrological tracing, while cobalt belongs to toxic heavy metals. The HQ was used to assess a series of human health risks. The HI values for adults and children are shown in Fig.14a and 14b, respectively.

For adults, HI values ranged from 0.01 to 4.12, with 11 out of 124 sampling sites (8.87%) exhibiting HI>1. For children, HI values ranged from 0.01 to 6.76, and 21 sites (16.94%) had HI>1. As shown in Tables S3 and S4, the contribution of individual trace elements to the total HI varied significantly. Mn and As were identified as the primary risk contributors.

For adults, Mn HI ranged from 0.00 to 3.51, with 3 sites exhibiting Mn HI>1. Children's HI values between 0.00 and 5.85, with 11 sites exhibiting Mn HI>1. Arsenic ranks second in terms of risk contribution. HI values ranged from 0.01 to 2.00 in adults and 0.00 to 3.00 in children. The spatial distribution of arsenic anomalies displays distinct regularities: all anomalous sites are distributed along the coastline(Figure S1). Interestingly, WQI screening identified three arsenic sites above limits, whereas HHRA detected five coastal locations with anomalous arsenic. This indicates that two sampling points satisfy the WQI threshold yet still pose non-carcinogenic health risks to children. These two sites meet WHO drinking water criteria but get flagged by HHRA methodology. The five coastal sites show vastly different hydrochemical conditions (saltwater intrusion, high alkalinity, reducing environments). Available data fail to identify a unified formation mechanism. Future work should include depth-profiled sampling, sediment mineralogy studies, and seasonal campaigns to clarify arsenic mobilization processes. Priority should be given to these coastal sites, especially since 40% of at-risk locations comply with WHO guidelines yet still pose child health threats. Contributions from other trace elements are minimal and can be considered negligible. One sample recorded a lead HI exceeding 1, though this appears to be an isolated case rather than a widespread issue.

Adult HI anomalies were concentrated in Chagan Town, Shantou City, and the western Pearl River Estuary. The spatial extent of childhood HI anomalies was broader, extending from Chagan Town toward central Jiangxi Province, from Shantou City northeastward to Xiamen and Quanzhou, and northward from the western Pearl River Estuary to Qingyuan. As shown in Fig.14, the total HI values for children exceeding 1 are mainly distributed in Cluster 1 and Cluster 3, with only a few occurrences in other clusters. For adults, sampling sites with total HI>1 are also predominantly located in Cluster 1 and Cluster 3, indicating elevated non-carcinogenic risks of trace elements in these areas. For both adults and children, the overall spatial distribution of high values is similar to that of WQI, suggesting that they are controlled by the same major influencing factors.

Further analysis of hazard indices via ingestion and dermal contact reveals that the health risk via ingestion is much higher than that via dermal contact. Abnormally high HQ values are mainly distributed in Cluster 1 and Cluster 3 for both adults and children. In addition, some exceptionally high HQ values for children appear in Cluster 5. Overall, the HQ and HI values for children are markedly higher than those for adults. This indicates that under identical groundwater exposure conditions, children are more susceptible to adverse health effects induced by trace elements at lower concentrations[133]. This sensitivity is related to children's physical development. Due to lower body weight, higher exposure dose per unit body weight, frequent hand-to-mouth behavior, immature organ development, and weak metabolic capacity, children face significantly higher health risks than adults under the same exposure level[134–136].


Legend
Cluster 1
Cluster 2
Cluster 3
Cluster 4
Cluster 5
Main city
HI
5
4
1
0.1
0
N
a)
b)
Chagan town
Zhangzhou
Quanzhou
Xiamen
Qingyuan
Zhaoqing
Guangzhou
Shantou
Zhongshan
Zhuhai
28°N
27°N
26°N
25°N
24°N
23°N
22°N
21°N
110°E
111°E
112°E
113°E
114°E
115°E
116°E
117°E
118°E
119°E
120°E

663

Figure 14. Human health risk spatial distribution in the study area. (a) HI distribution map for adults; (b) HI distribution map for children.

Integrated Analysis of WQI and HHRA

Both assessments converge on the same high-risk zones. Elevated WQI values and elevated HI values exhibit extensive spatial overlap.This spatial overlap is not coincidental but reflects a shared geochemical driver: Mn enrichment. This spatial co-occurrence provides independent corroboration that Mn enrichment is the primary driver, as two structurally distinct assessment frameworks converge on the same geographic loci.

Despite their spatial consistency, the two methods differ considerably in detection sensitivity. WQI identified 4.84% of samples as having unacceptable water quality (WQI > 100), whereas HHRA flagged 8.87% of adult sites and 16.94% of children's sites as exceeding the non-carcinogenic risk threshold (HI > 1). The increase in outlier values stems from discrepancies in the principles of the two detection methods. HHRA can catch situations that slip through standard testing. When individual elements stay within safe limits, their combined presence at medium levels can still create real health risks.

Arsenic serves as a highly representative example. In the WQI analysis, only 3 arsenic values exceeded the standard which exerting minimal influence on the overall WQI. In contrast, HHRA ranked arsenic as the second most significant factor after manganese. At sites with the highest arsenic concentrations, the As HI reached 2.0 for adults and 3.0 for children. This reveals that even when arsenic concentrations fall below the WQI threshold, significant toxicological hazards still exist when evaluated via the dose-based health risk assessment framework. HHRA reveals risks that WQI fails to detect, underscoring the importance of applying both assessment methods concurrently.

Another limitation of WQI is its inability to differentiate risks according to population characteristics. Among all study sites, HI values for children were significantly higher than those for adults, reaching a maximum of 6.76 compared to only 4.12 for adults. For monitoring points, the proportion of sites where children's HI exceeded 1 was 16.94%, nearly double the adult proportion of 8.87%. Moreover, the areas where children's HI exceeded thresholds was considerably more extensive, stretching from the core anomaly zone through Jiangxi Province, most of Fujian Province, and into the northern Pearl River Delta region. These findings carry direct implications for public health management. In areas where groundwater serves as the primary water source, children should be recognized as a priority vulnerable group. Relevant regulatory measures should be established based on protective exposure thresholds for children rather than average values for the general population.

Overall, WQI and HHRA are not redundant but complementary. WQI provides a rapid screening tool well suited for large scale of spatial assessments. HHRA offers a mechanistic and sensitive risk evaluation method that is better suited for identifying cumulative health risks and unique health vulnerabilities across different population groups.

Water quality monitoring and management strategies

The assessments above show that the risk patterns vary widely across different areas so that different management approaches are needed. In terms of concentration alone, over 90% of water bodies meet the safe drinking water standards. However, the situation changes when modeling cumulative dose exposure. Risk rates are 9% for adults and 17% for children, and these

rates grow over time. Such spatial heterogeneity necessitates the establishment of a hierarchical management system tailored to local pollution levels and the characteristics of susceptible populations.

High-priority zones need more intensive monitoring. Quarterly sampling should focus on Mn and As, with more frequent checks during monsoon seasons when mobilization risk is highest. Wells in these areas that serve over 500 people need immediate hazard reviews using child-based exposure parameters.

Removing existing heavy metal contamination requires the right treatment methods. For household or small systems, catalytic oxidation combined with granular adsorption filtration works well and costs less. For large supply networks, newer membrane technologies offer solid options. Coastal areas affected by seawater intrusion also need a different approach.Given the mixing characteristics of seawater and freshwater in these areas, the optimal strategy lies in optimizing freshwater recharge rather than attempting to treat seawater sources. In areas with geothermal resources but poor water quality, non-contact use makes more sense than treating water to drinking standards.

Effective remediation hinges on a sound management system. Annual assessment of high-risk areas using both concentration limits and dose-related indicators can verify the effectiveness of remediation interventions and facilitate timely detection of emerging pollution. The formulation of these indicators and regulations, implemented by provincial health and environmental authorities, should establish special protective threshold standards for children for public healthcare systems serving child-concentrated areas. Using community publicity campaigns in Mandarin and local dialects will improve compliance with advisories and treatment recommendations, especially in rural areas where private wells are common. Investing in regional monitoring networks that track water levels, temperature, and multiple hydrochemical parameters will give early warning of emerging contamination or aquifer stress. This allows managers to act proactively instead of just reacting to problems.

Conclusion

Combined with SOM-KM clustering analysis, PCA, basic hydrochemical analysis, WQI and HHRA, this study systematically evaluated the water quality characteristics, sources and related health risks of groundwater in Guangdong and Fujian. The main conclusions are summarized as follows:

1. Hydrochemical analysis reveals groundwater sources. SOM-KM analysis divided 124 samples into five clusters. Cluster 1 (Ca-HCO3 and mixed Ca-Na-HCO3 types) comes from cold groundwater in areas where carbonate and silicate rocks weather together. Halite and K-Na feldspar dissolve here, which causes positive cation exchange. Cluster 2 (Na-HCO3 and Na-Cl types) is thermal groundwater. Higher temperatures increase evaporative concentration and silicate weathering, which are the main sources, with some gypsum dissolution as well. Cluster 3 (Na-Cl type) shows strong evaporite dissolution caused by heavy evaporation, along with reverse cation exchange. Cluster 4 (Na-Cl type) is mainly influenced by seawater intrusion, which stable isotope data confirm through deviations from the meteoric water line. Cluster 5 (mixed type) has a scattered pattern, probably due to atmospheric deposition mixed with weak cation exchange. PCA identified four main components: natural water-rock interaction (PC1), weakly alkaline ionic synergy (PC2), high-temperature mineral dissolution (PC3), and pH-controlled arsenic

mobilization (PC4). Stable isotope data show that meteoric precipitation is the primary recharge source for all clusters, with Cluster 4 being the exception.

2. Among the study area, water quality is far from uniform, and the contamination patterns that emerge appear closely tied to local hydrogeochemical conditions. Mn enrichment is the most pressing concern. Roughly 90% of sampling sites still fall within acceptable drinking water limits, but a number of hotspots recorded strikingly elevated Mn concentrations. In the north-central carbonate-silicate transition zone, anoxic conditions drive reductive dissolution of Mn-bearing minerals, while in the organic-rich coastal sediments further south, sulfate reduction takes over as the dominant process. The tendency for high WQI values and Mn anomalies to cluster in the same locations points clearly to natural redox-sensitive processes rather than anthropogenic pollution as the underlying cause. For rural populations in northern Guangdong that rely on shallow cold groundwater, this is a practical concern: long residence times and sparse recharge allow Mn to accumulate to problematic levels over time.

3. Among all detected contaminants, Mn also emerges as the dominant driver of non-carcinogenic risk, affecting 16.94% of sites for children compared to 8.87% for adults. In Cluster 1, where reductive dissolution appears to sustain persistently high Mn concentrations, individual HI values reached as high as 5.85. By contrast, As presents more localized concerns, mainly in coastal areas.

Comparing the two assessment approaches reveals an interesting pattern. Three of the five flagged sites showed abnormalities under both WQI and HHRA, while the remaining two were only caught by HHRA, where arsenic HI values for children already exceeded the safe threshold. This suggests that HHRA is the more sensitive of the two tools. The proportion of unacceptable samples is 4.8% based on WQI, while the unacceptable proportion for children reaches as high as 17% under HHRA, which reflects the fundamental differences between the two assessment methods. WQI applies single-element thresholds and misses the compounding effects of simultaneous exposure to multiple constituents. HHRA accounts for these cumulative burdens and also distinguishes between receptor groups. Children bear a disproportionate share of the risk, facing nearly twice the exceedance rate of adults. Part of this discrepancy arises from children's lower body weight and weaker detoxification capacity; another contributing factor is that high-risk zones extend beyond the core anomalous belts to surrounding areas.

The north-central carbonate-silicate transition zone stands out as a clear priority for intervention, given that elevated HI values, poor WQI scores, and Cluster 1 hydrochemistry all concentrate in the same area. Protecting children in this region will require targeted measures, including seasonal Mn monitoring during wet periods when reductive leaching intensifies, and practical alternatives to shallow groundwater such as rainwater harvesting or piped supply networks for rural households. Taken together, these findings reinforce the value of using WQI and HHRA in tandem: the former offers a fast, regulation-based screening tool, while the latter provides a more mechanistic and receptor-sensitive lens that standard water quality criteria alone cannot replicate.

References

1. Barbier, E. Geothermal energy technology and current status: an overview. *Renewable and Sustainable Energy Reviews* **6**, 3–65 (2002).
2. Borovic, S. & Markovic, I. Utilization and tourism valorisation of geothermal waters in Croatia. *Renewable and Sustainable Energy Reviews* **44**, 52–63 (2015).

3. Carrera-Villacres, D., Guevara-Garcia, P., Hidalgo-Hidalgo, A., Teresa-Vivero, M. & Maya-Carrillo, M. Removal of Physical Information Chemistry of Spa that is Utilizing Geothermal Water in Ecuador. *Procedia Earth and Planetary Science* **15**, 367–373 (2015).
4. Oyuntsetseg, D., Ganchimeg, D., Minjigmaa, A., Ueda, A. & Kusakabe, M. Isotopic and chemical studies of hot and cold springs in western part of Khangai Mountain region, Mongolia, for geothermal exploration. *Geothermics* **53**, 488–497 (2015).
5. Tomaszewska, B. *et al.* Utilization of renewable energy sources in desalination of geothermal water for agriculture. *Desalination* **513**, 115151 (2021).
6. Chalise, B. *et al.* Water quality and hydrochemical assessments of thermal springs, Gandaki Province, Nepal. *Heliyon* **9**, e17353 (2023).
7. Fan, W. *et al.* Hydrochemical characteristics, control factors and health risk assessment of groundwater in typical arid region Hotan Area, Chinese Xinjiang. *Environmental Pollution* **363**, 125301 (2024).
8. Ma, W., Peng, C., Ahmed, S. F., Yang, C. & Liu, G. Assessment of geothermal water environment using multi-influencing factor analysis method: A case study of Reshuiwei geothermal field. *Physics and Chemistry of the Earth, Parts A/B/C* **139**, 103896 (2025).
9. Rabbani, O. *et al.* Spatial distribution, potential health risks, and sources of groundwater contamination in the semi-arid region. *Physics and Chemistry of the Earth, Parts A/B/C* **139**, 103952 (2025).
10. Liu, L. *et al.* Global characteristics of drought propagation from surface water to groundwater. *Journal of Hydrology* **665**, 134734 (2026).
11. Su, X. *et al.* Groundwater environmental risk early warning based on a novel model in western Songnen Plain, China. *Journal of Hydrology* **664**, 134537 (2026).
12. Mjami, N. B., Kimambo, C., Ayeng'o, S. & Orozova-Bekkevold, I. Prospects and challenges for utilisation of low- to medium-temperature geothermal resources in Tanzania. *Geothermics* **129**, 103288 (2025).
13. Wen, C. *et al.* Hydrochemical characteristics and circulation pattern of fault-type geothermal water in karst region: A case study in western Yunnan, China. *Geothermics* **132**, 103432 (2025).
14. Famiglietti, J. S. The global groundwater crisis. *Nature Climate Change* **4**, 945–948 (2014).
15. Zheng, H. & Luo, J. Progress in research on the exploration and evaluation of deep geothermal resources in the Fujian-Guangdong-Hainan region, China. *Energy Geoscience* **5**, 100232 (2024).
16. Hao, M. *et al.* Study on the Genetic Mechanism of Carbonate Rock Type Hot Mineral Water─A Case Study of Diaozhen, Jinan. *ACS Omega* **9**, 26458-26471 (2024).
17. Lei, Y. *et al.* Hydrogeochemical and isotopic analysis for interpreting the formation of the complex geothermal system in the Guide Basin, Northeastern Tibetan Plateau. *PLOS ONE* **20**, e0317694 (2025).
18. Tamburello, G. *et al.* Global thermal spring distribution and relationship to endogenous and exogenous factors. *Nature Communications* **13**, 6378 (2022).
19. He, Z., Feng, J., Luo, J. & Zeng, Y. Distribution, exploitation, and utilization of intermediate-to-deep geothermal resources in eastern China. *Energy Geoscience* **4**, 100187 (2023).
20. Leal-Acosta, M. L. *et al.* Intertidal geothermal hot springs as a source of trace elements to the coastal zone: A case study from Bahía Concepción, Gulf of California. *Marine Pollution Bulletin* **128**, 51–64 (2018).
21. Wei, Z. *et al.* Geochemical evolution of geothermal waters in the Pearl River Delta region, South China: Insights from water chemistry and isotope geochemistry. *Journal of Hydrology: Regional Studies* **51**, 101670 (2024).
22. Huang, H. *et al.* Hydrochemical evolution and genesis of geothermal waters in the Cuona-Woka rift zone of Southern Tibet, Southwestern China. *Environmental Earth Science* **84**, 163 (2025).
23. Shintani, T., Tomita, K. & Morikawa, N. Estimation of flow dynamics of saline groundwater in a coastal geothermal region based on B–Li–Cl classification and geochemical measurements. *Applied Geochemistry* **195**, 106625 (2025).
24. Shi, X. *et al.* Hydrochemistry and isotope geochemistry of Bailing geothermal water in northwest Jiangxi: Implications for water-rock interaction. *Geothermics* **131**, 103402 (2025).
25. Wei, D. *et al.* Appraisal of potential toxic elements pollution, sources apportionment, and health risks in groundwater from a coastal area of SE China. *Journal of Environmental Management* **377**, 124691 (2025).
26. Cheng, Z. *et al.* Hydrogeological flow patterns and hydrochemical driving forces of groundwater in a typical coastal hilly region of the Jinjiang watershed, Southeast China: Recommendations for water pollution control and management. *China Geology* **9**, 316–332 (2026).
27. Nowicki, S. *et al.* Water chemistry poses health risks as reliance on groundwater increases: A systematic review of hydrogeochemistry research from Ethiopia and Kenya. *Science of The Total Environment* **904**, 166929 (2023).

28. Liu, Y., Zhou, L., Ma, X., Li, W. & Li, J. Comprehensive Study of Groundwater Hydrochemistry, Driving Forces, and Health Risks in Representative Rural Agglomerations, Northern China. *ACS Omega* **10**, 18391–18403 (2025).
29. Fu, J. *et al.* Integrating hydrogeochemical characterization and multivariate statistics for the source identification and health risk assessment of groundwater pollution in the Ze Zhou Basin, Northern China. *Environmental Pollution* **383**, 126833 (2025).
30. Gupta, S. & Maiti, S. Groundwater quality and fluoride contamination risks in Jharkhand state: A regional IWQI analysis and hydrochemistry insights. *Journal of Environmental Chemical Engineering* **13**, 118253 (2025).
31. Li, Q., Kang, X., Xu, M., Wang, D. & Li, K. Groundwater quality and risk assessment in urban areas of arid regions on the western Qinghai-Tibet Plateau. *Groundwater for Sustainable Development* **31**, 101547 (2025).
32. Takeya, L. A. *et al.* Hydrochemistry, quality, and potential health risk appraisal of arsenic-enriched groundwater in central-west Bangladesh using the integrated water quality index and Monte Carlo simulation. *Science of The Total Environment* **1003**, 180707 (2025).
33. Kang, D. *et al.* Identification and assessment of urban groundwater pollution based on Monte Carlo health risk modeling and self-organizing map (SOM). *Journal of Contaminant Hydrology* **277**, 104807 (2026).
34. Liang, S. *et al.* Steep subduction of the Indian continental mantle lithosphere beneath the eastern Himalaya revealed by gravity anomalies. *Science China Earth Science* **66**, 1994–2010 (2023).
35. El-Rawy, M. *et al.* Assessment of groundwater quality in arid regions utilizing principal component analysis, GIS, and machine learning techniques. *Marine Pollution Bulletin* **205**, 116645 (2024).
36. Samadi, J. Modelling hydrogeological parameters to assess groundwater pollution and vulnerability in Kashan aquifer: Novel calibration-validation of multivariate statistical methods and human health risk considerations. *Environmental Research* **211**, 113028 (2022).
37. Zhang, W., Peng, J. & Liu, Y. Hydrogeochemical Characteristics of the Geothermal System in the Woka-Cuona Rift Zone, Tibet. *Water* **16**, 1395 (2024).
38. Ravindiran, G. *et al.* Study on hydrogeochemical assessment, groundwater quality index for drinking, seawater mixing index and human health risk assessment of nitrate and fluoride. *Groundwater for Sustainable Development* **25**, 101161 (2024).
39. Rehman, N. ur *et al.* Assessment of water quality and health hazards using water quality index and human health risk evaluation in district Talagang Pakistan. *Scientific Reports* **15**, 5191 (2025).
40. Nasim, I. *et al.* Water quality index and human health risk analysis in urban drinking water sources. *Scientific Reports* **16**, 12831 (2026).
41. Xu, N. *et al.* Occurrence and enrichment mechanism of arsenic-rich groundwater from eastern coastal China. *Groundwater for Sustainable Development* **27**, 101385 (2024).
42. Cai, Y., Liu, C., Cao, S., Li, J. & Dong, Y. Hydrochemical evolution of hydrothermal systems driven by seawater mixing in the southeastern coastal region of China: insights from water chemistry and isotopes. *Geothermics* **136**, 103616 (2026).
43. Han, D. & Currell, M. J. Review of drivers and threats to coastal groundwater quality in China. *Science of The Total Environment* **806**, 150913 (2022).
44. Yuan, J., Xu, F. & Zheng, T. The genesis of saline geothermal groundwater in the coastal area of Guangdong Province: Insight from hydrochemical and isotopic analysis. *Journal of Hydrology* **605**, 127345 (2022).
45. Ding, R., Zhang, K., Min, K. & Zou, H. Reconstruction of the topographic evolution of the Nanling Range in South China and its implications for the East Asian Monsoon evolution. *Palaeogeography, Palaeoclimatology, Palaeoecology* **634**, 111947 (2024).
46. Feng, J. Factors controlling the distribution of granite reservoirs of hydrothermal system type in South China: A case study of Huangshadong geothermal field in Yuezhong Depression, China. *Energy Geoscience* **4**, 100160 (2023).
47. Li, Z.X. & Li, X.H. Formation of the 1300-km-wide intracontinental orogen and postorogenic magmatic province in Mesozoic South China: A flat-slab subduction model. *Geology* **35**, 179–182 (2007).
48. Zhang, G. *et al.* Tectonics of South China continent and its implications. *Science China Earth Science* **56**, 1804–1828 (2013).
49. Mao, J., Li, Z. & Ye, H. Mesozoic tectono-magmatic activities in South China: Retrospect and prospect. *Science China Earth Sciences* **57**, 2853–2877 (2014).
50. Li, Y., He, R., Wang, B., Niu, X. & Li, Z. Pn velocity and anisotropy at the lithospheric mantle wedge beneath the middle-eastern Gangdese Metallogenic Belt, southern Tibet, China. *Journal of Asian Earth Sciences* **258**, 105633 (2023).

51. Li, J., Xie, X. & Wang, Y. Effects of the groundwater flowing and redox conditions on arsenic mobilization in aquifers of the Datong Basin, Northern China. *Journal of Hydrology* **636**, 131256 (2024).
52. Huang, Z. *et al.* Notably high salinity of geothermal water in the coastal area in Hainan Island, China, predominantly dominated by tectonic activities. *Geothermics* **126**, 103202 (2025).
53. Liu, Y. *et al.* The Genesis and Circulation of Geothermal Water in the Riduo–Cuona Rift, Eastern Tibetan Plateau, Based on Hydrochemistry and Stable Isotopes Geochemistry. *Geological Journal* **60**, 642–658 (2025).
54. Zhou, X.M., Sun, T., Shen, W.Z., Shu, L.S. & Niu, Y. Petrogenesis of Mesozoic granitoids and volcanic rocks in South China: A Response to Tectonic Evolution. *Episodes* **29**, (2006).
55. Wang, H., Mao, X., Li, C., Dong, Y. & Ye, J. An additional source for the hydrochemical formation of geothermal waters in granites. *Geothermics* **114**, 102793 (2023).
56. Hao, A. *et al.* Review: Groundwater resources and related environmental issues in China. *Hydrogeol J* **26**, 1325–1337 (2018).
57. Zheng, Y. *et al.* Hydrochemical insights, water quality, and human health risk assessment of groundwater in a coastal area of southeastern China. *Environmental Monitoring and Assessment* **196**, 959 (2024).
58. Lancia, M. *et al.* Hydrogeology of the Pearl River Delta, southern China. *Journal of Maps* **16**, 388–395 (2020).
59. Sheng, C. *et al.* Offshore freshened groundwater in the Pearl River estuary and shelf as a significant water resource. *Nature Communication* **14**, 3781 (2023).
60. Sheng, C. *et al.* Evolution of groundwater system in the Pearl River Delta and its adjacent shelf since the late Pleistocene. *Science Advances* **10**, eadn3924 (2024).
61. Wang, Z. *et al.* Structure identification of a karst groundwater system based on high-resolution rainfall-hydrological response characteristics. *Environmental Science Pollution Research* **29**, 26922–26935 (2022).
62. Changsong Z. *et al.* Key technical points for integrated surface water-groundwater surveys and assessment in karst basins of South China. *zgyr* **44**, 912–927 (2025).
63. Liu, B., Peng, S., Liao, Y. & Wang, H. The characteristics and causes of increasingly severe saltwater intrusion in Pearl River Estuary. *Estuarine, Coastal and Shelf Science* **220**, 54–63 (2019).
64. Yao, B. et al. Environmental geochemical characteristics of hot springs in fault zone in Fujian. *Environmental Chemistry* **43**, 2356–2372 (2024).
65. Güler, C., Thyne, G. D., McCray, J. E. & Turner, K. A. Evaluation of graphical and multivariate statistical methods for classification of water chemistry data. *Hydrogeology Journal* **10**, 455–474 (2002).
66. Woith, H., Wang, R., Maiwald, U., Pekdeger, A. & Zschau, J. On the origin of geochemical anomalies in groundwaters induced by the Adana 1998 earthquake. *Chemical Geology* **339**, 177–186 (2013).
67. Parisi, A., Alfio, M. R., Balacco, G., Güler, C. & Fidelibus, M. D. Analyzing spatial and temporal evolution of groundwater salinization through Multivariate Statistical Analysis and Hydrogeochemical Facies Evolution-Diagram. *Science of The Total Environment* **862**, 160697 (2023).
68. Chen, K., Liu, Q., Peng, W. & Liu, X. Source apportionment and natural background levels of major ions in shallow groundwater using multivariate statistical method: A case study in Huaibei Plain, China. *Journal of Environmental Management* **301**, 113806 (2022).
69. Kim, K.H. *et al.* Geochemical pattern recognitions of deep thermal groundwater in South Korea using self-organizing map: Identified pathways of geochemical reaction and mixing. *Journal of Hydrology* **589**, 125202 (2020).
70. Yang, Y., Wang, C., Guo, H., Sheng, H. & Zhou, F. An integrated SOM-based multivariate approach for spatio-temporal patterns identification and source apportionment of pollution in complex river network. *Environmental Pollution* **168**, 71–79 (2012).
71. Lee, K.J. *et al.* The combined use of self-organizing map technique and fuzzy c-means clustering to evaluate urban groundwater quality in Seoul metropolitan city, South Korea. *Journal of Hydrology* **569**, 685–697 (2019).
72. Haselbeck, V., Kordilla, J., Krause, F. & Sauter, M. Self-organizing maps for the identification of groundwater salinity sources based on hydrochemical data. *Journal of Hydrology* **576**, 610–619 (2019).
73. Liu, Z., Feng, S., Zhangsong, A., Han, Y. & Cao, R. Long-term evolution of groundwater hydrochemistry and its influencing factors based on self-organizing map (SOM). *Ecological Indicators* **154**, 110697 (2023).
74. Sinaga, K. P. & Yang, M.-S. Unsupervised K-Means Clustering Algorithm. *IEEE Access* **8**, 80716–80727 (2020).

75. Najafi Neysiani, S., Roozbahani, A., Javadi, S. & Hashemy Shahdany, S. M. Water resources assessment of zayandeh-rood river basin using integrated surface water and groundwater footprints and K-means clustering method. *Journal of Hydrology* **614**, 128549 (2022).
76. Zhou, Z., Chen, M. & Li, Y. Source apportionment of groundwater contamination using integrated PCA-APCS-MLR modeling: A case study of an industrial zone in Southwest China. *Environmental Research* **292**, 123628 (2026).
77. Nadjet, Z. *et al.* Multivariate analysis of groundwater quality using PCA and HAC: Geochemical controls on mineralization, nitrification, and pollutant dynamics in southeastern Arid Region of Algeria. *Desalination and Water Treatment* **324**, 101463 (2025).
78. Helsel, D.R. More Than Obvious: Better Methods for Interpreting Nondetect Data. *Environmental Science & Technology Journal* **39**, 419A-423A (2005).
79. Hedayatpour, M., Rabieifar, H., Darvishi, H. H., Shirinabadi, R. & Farokhizadeh, S. Assessment of groundwater quantity and quality indexes and WQI determination for drinking and agricultural uses: Alborz Plain, Iran case study. *Alexandria Engineering Journal* **134**, 391–416 (2026).
80. Chidiac, S., El Najjar, P., Ouaini, N., El Rayess, Y. & El Azzi, D. A comprehensive review of water quality indices (WQIs): history, models, attempts and perspectives. *Reviews Environmental Science and Bio/technology* **22**, 349–395 (2023).
81. Na, J., Cen, C., Shi, Z. & Feng, B. Distinct response of deep and shallow geothermal reservoir temperature following earthquakes in the Kangding Fault zone hydrothermal system. *Journal of Hydrology: Regional Studies* **52**, 101743 (2024).
82. Masoud, A. M. & Ali, M. H. Coupled multivariate statistical analysis and WQI approaches for groundwater quality assessment in Wadi El-Assiuty downstream area, Eastern Desert, Egypt. *Journal of African Earth Sciences* **172**, 103982 (2020).
83. Kalaivanan, K. *et al.* Groundwater quality and nitrate health risk evaluation in eastern part of Salem district, South India: Insights from water quality index (WQI) and GIS techniques. *Journal of Environmental Chemical Engineering* **13**, 118609 (2025).
84. Pattnayak, S., Karmakar, S. & Mukherji, S. An integrated assessment and visualization framework combining PCA-weighted WQI and human health hazard index to map groundwater hotspots: Evidence from Maharashtra, India. *Environmental Research* **298**, 124245 (2026).
85. Şener, Ş., Şener, E. & Davraz, A. Evaluation of water quality using water quality index (WQI) method and GIS in Aksu River (SW-Turkey). *Science of The Total Environment* **584–585**, 131–144 (2017).
86. Vystavna, Y., Harjung, A., Monteiro, L. R., Matiatos, I. & Wassenaar, L. I. Stable isotopes in global lakes integrate catchment and climatic controls on evaporation. *Nature Communications* **12**, 7224 (2021).
87. Dong, H. *et al.* Hydrogeochemical characteristics of hot springs in the Daju Fault Zone of the SE Tibetan Plateau, China. *Journal of Asian Earth Sciences* **278**, 106398 (2025).
88. Zhang, Y. *et al.* Hydrogeochemical analysis and groundwater pollution source identification based on self-organizing map at a contaminated site. *Journal of Hydrology* **616**, 128839 (2023).
89. Al Maliki, A. *et al.* Geochemical processes, salinity sources and utility characterization of groundwater in a semi-arid region of Iraq through geostatistical and isotopic techniques. *Environmental Monitor and Assessment* **196**, 365 (2024).
90. Abdelfadel, F. *et al.* Tracing groundwater's footprint in African semi-arid lands: isotopic tools for aquifer management. *Hydrological Sciences Journal* **70**, 2745–2761 (2025).
91. Du, C. *et al.* Stable Isotope Characteristics and Recharge Mechanisms of River, Lake and Groundwater by Precipitation in the Hulun Lake Basin. *Hydrological Processes* **39**, e70174 (2025).
92. Sulca, P. *et al.* An Integrated Analysis to Delineate Groundwater Flow Systems and Recharge Dynamics in the Chili River Sub-Basin, Southern Peru. *Water* **18**, 667 (2026).
93. Guo, L., Wang, G., Sheng, Y. & Shi, Z. Hydrogeochemical Constraints Shape Hot Spring Microbial Community Compositions: Evidence From Acidic, Moderate-Temperature Springs and Alkaline, High-Temperature Springs, Southwestern Yunnan Geothermal Areas, China. *Journal of Geophysical Research: Biogeosciences* **126**, e2020JG005868 (2021).
94. Pang, Z., Kong, Y., Li, J. & Tian, J. An Isotopic Geoindicator in the Hydrological Cycle. *Procedia Earth and Planetary Science* **17**, 534–537 (2017).
95. Jie, H. *et al.* Seasonality of precipitation isotopes associated with water vapor budget: A hierarchical clustering-based zoning in China. *Atmospheric Research* **317**, 107970 (2025).
96. Qu, S. *et al.* Hydrochemical assessments and driving forces of groundwater quality and potential health risks of sulfate in a coalfield, northern Ordos Basin, China. *Science of The Total Environment* **835**, 155519 (2022).

97. Xiao, Y. *et al.* Investigating sources, driving forces and potential health risks of nitrate and fluoride in groundwater of a typical alluvial fan plain. *Science of The Total Environment* **802**, 149909 (2022).
98. Das, R., Subba Rao, N., Sahoo, H. K. & Sakram, G. Nitrate contamination in groundwater and its health implications in a semi-urban region of Titrol block, Jagatsinghpur district, Odisha, India. *Physics and Chemistry of the Earth, Parts A/B/C* **132**, 103424 (2023).
99. Wen, S. *et al.* Hydrochemical Characteristics and Evolution Mechanisms of Shallow Groundwater in the Alluvial–Coastal Transition Zone of the Tangshan Plain, China. *Water* **17**, 2810 (2025).
100. Carol, E., Kruse, E. & Mas-Pla, J. Hydrochemical and isotopical evidence of ground water salinization processes on the coastal plain of Samborombón Bay, Argentina. *Journal of Hydrology* **365**, 335–345 (2009).
101. Tang, L. *et al.* Hydrochemical analysis and groundwater suitability for drinking and irrigation in an arid agricultural area of the Northwest China. *Journal of Contaminant Hydrology* **259**, 104256 (2023).
102. Brhane, G. K. & Mekonen, H. S. Identifying controlling factors for the evolution of shallow groundwater chemistry of Ellala catchment, northern Ethiopia. *Sustainable Water Resources Management* **10**, 62 (2024).
103. Gaillardet, J., Dupré, B., Louvat, P. & Allègre, C. J. Global silicate weathering and CO2 consumption rates deduced from the chemistry of large rivers. *Chemical Geology* **159**, 3–30 (1999).
104. Obeidat, M. & Awawdeh, M. Assessment of groundwater quality in the area surrounding Al-Zaatari Camp, Jordan, using cluster analysis and water quality index (WQI). *The Jordan Journal of Earth Environmental Science* **12**, 187–197 (2021).
105. Hem, J. D. Manganese Complexes with Bi-Carbonate and Sulfate in Natural Water. *Journal of Chemical & Engineer Data* **8**, 99–101 (1963).
106. Kiracofe, Z. A., Henika, W. S. & Schreiber, M. E. Assessing the Geological Sources of Manganese in the Roanoke River Watershed, Virginia. *Environmental & Engineering Geoscience* **23**, 43–64 (2017).
107. Zhao, M. *et al.* Anthropogenic perturbation enhances the release of geogenic Mn to groundwater: Evidence from hydrogeochemical characteristics. *Science of The Total Environment* **891**, 164450 (2023).
108. Ayoob, S. & Gupta, A. K. Fluoride in Drinking Water: A Review on the Status and Stress Effects. *Critical Reviews in Environmental Science and Technology* **36**, 433–487 (2006).
109. Wang, C.Y., Meng, E., Lin, S. & Li, Y.G. Late Neoarchean metavolcanic rocks from the Tonghua area, Southern Jilin Province, China: Constraints on the formation and evolution of the northeastern North China Craton. *Precambrian Research* **362**, 106266 (2021).
110. Edmunds, W. M. & Smedley, P. L. Fluoride in Natural Waters. in *Essentials of Medical Geology: Revised Edition* (ed. Selinus, O.) 311–336 (Springer Netherlands, Dordrecht, 2013). doi:10.1007/978-94-007-4375-5_13.
111. Meenakshi, Garg, V. K., Kavita, Renuka & Malik, A. Groundwater quality in some villages of Haryana, India: focus on fluoride and fluorosis. *Journal of Hazardous Materials* **106**, 85–97 (2004).
112. Gomez, M. L., Blarasin, M. T. & Martínez, D. E. Arsenic and fluoride in a loess aquifer in the central area of Argentina. *Environmental Geology* **57**, 143–155 (2009).
113. Liu, M., Guo, Q., Zhang, X. & Wang, Y. Characteristic solutes in geothermal water from the Rehai hydrothermal system, Southwestern China. *Journal of Earth Science* **26**, 140–148 (2015).
114. Han, B. *et al.* Fluorite deposits in China: Geological features, metallogenic regularity, and research progress. *China Geology* **3**, 473–489 (2020).
115. He, X. *et al.* Groundwater Arsenic and Fluoride and Associated Arsenicosis and Fluorosis in China: Occurrence, Distribution and Management. *Exposure Health* **12**, 355–368 (2020).
116. Cao, H., Xie, X., Wang, Y. & Deng, Y. The interactive natural drivers of global geogenic arsenic contamination of groundwater. *Journal of Hydrology* **597**, 126214 (2021).
117. Williamson, A. J. *et al.* Microbial Reduction of Fe(III) under Alkaline Conditions Relevant to Geological Disposal. *Applied and Environmental Microbiology* **79**, 3320–3326 (2013).
118. Tian, J. *et al.* Earthquake-induced impulsive release of water in the fractured aquifer system: Insights from the long-term hydrochemical monitoring of hot springs in the Southeast Tibetan Plateau. *Applied Geochemistry* **148**, 105553 (2023).
119. He, P. *et al.* Geological and hydrochemical controls on water chemistry and stable isotopes of hot springs in the Three Parallel Rivers Region, southeast Tibetan Plateau: The genesis of geothermal waters. *Science of The Total Environment* **906**, 167648 (2024).
120. Husain, M. S., Ahmad, I. & Umar, R. Hydrochemistry, controlling mechanisms and water quality index in hot springs of the Kullu-Manali region, India. *Groundwater for Sustainable Development* **24**, 101070 (2024).

121. Roy, S., Kumar, B., Chowdhury, A., Singh, U. K. & Ray, S. Characterization of hydrogeochemical process and evaluation of water quality of seven geothermal springs, Bakreswar, India. *Arabian Journal of Geosciences* **11**, 314 (2018).
122. Hanxiong, Z., Guiling, W., Wei, Z. & Mengmeng, W. Characterization of geothermal water-rock interaction processes and transport patterns using geochemical methods. *Geochemistry* **86**, 126389 (2026).
123. Ma, A. *et al.* "Mn(II) Curtain" in the riparian sediment at the lower reaches of the Hanjiang River, China. *Journal of Hydrology* **625**, 130047 (2023).
124. Phillips, A. H. Isomorphous substitution of elements in minerals *. *American Mineralogist* **17**, 85–93 (1932).
125. Xu, F. & Li, P. Biogeochemical mechanisms of iron (Fe) and manganese (Mn) in groundwater and soil profiles in the Zhongning section of the Weining Plain (northwest China). *Science of The Total Environment* **939**, 173506 (2024).
126. Ramachandran, M., Schwabe, K. A. & Ying, S. C. Shallow Groundwater Manganese Merits Deeper Consideration. *Environmental Science & Technology Journal* **55**, 3465–3466 (2021).
127. Ji, H. *et al.* Geochemical and hydrological processes control the distribution of high iron and manganese concentrations in groundwater within quaternary aquifers. *Journal of Hydrology* **663**, 134063 (2025).
128. Church, C. D., Wilkin, R. T., Alpers, C. N., Rye, R. O. & McCleskey, R. B. Microbial sulfate reduction and metal attenuation in pH 4 acid mine water. *Geochemical Transaction* **8**, 10 (2007).
129. Fh, C., Pm, B., Ma, T. & Pb, M. Distinguishing iron-reducing from sulfate-reducing conditions. *Ground water* **47**, (2009).
130. Frisbie, S. H., Mitchell, E. J., Dustin, H., Maynard, D. M. & Sarkar, B. World Health Organization Discontinues Its Drinking-Water Guideline for Manganese. *Environmental Health Perspectives* **120**, 775–778 (2012).
131. Rutchik, J. S., Zheng, W., Jiang, Y. & Mo, X. How Does an Occupational Neurologist Assess Welders and Steelworkers for a Manganese-Induced Movement Disorder? An International Team's Experiences in Guanxi, China, Part I. *Journal of Occupational and Environmental Medicine* **54**, 1432–1434 (2012).
132. Sharma, G. K. *et al.* Evaluating the geochemistry of groundwater contamination with iron and manganese and probabilistic human health risk assessment in endemic areas of the world's largest River Island, India. *Environmental Toxicology and Pharmacology* **87**, 103690 (2021).
133. Wu, J. & Sun, Z. Evaluation of Shallow Groundwater Contamination and Associated Human Health Risk in an Alluvial Plain Impacted by Agricultural and Industrial Activities, Mid-west China. *Exposure Health* **8**, 311–329 (2016).
134. Chen, J., Wu, H., Qian, H. & Gao, Y. Assessing Nitrate and Fluoride Contaminants in Drinking Water and Their Health Risk of Rural Residents Living in a Semiarid Region of Northwest China. *Exposure Health* **9**, 183–195 (2017).
135. Zhai, Y. *et al.* Groundwater nitrate pollution and human health risk assessment by using HHRA model in an agricultural area, NE China. *Ecotoxicology and Environmental Safety* **137**, 130–142 (2017).
136. Talib, M. A., Wahab, A., Usman, M., Sohail, M. T. & Ali, M. R. Groundwater governance: Integrating HHRA and strategic foresight to mitigate arsenic risk in Central Sindh, Pakistan. *Futures* **176**, 103761 (2026).

Funding and Conflicts of interests

The work was funded by Basic Scientific Research Fund of Institute of Earthquake Forecasting, China Earthquake Administration (CEAIEF2025080102, CEAIEF20250601, CEAIEF2025030101), Deep Earth Probe and Mineral Resources Exploration National Science and Technology Major Project (2024ZD1000500, 2025ZD1005100, 2025ZD1010303), the National Natural Science Foundation of China (41673106, W2412057), IGCP Project 724.

The authors declare no competing interests.

Author contributions statement

R.L. : Conceptualization, Methodology, Investigation, Writing-original draft, Writing-review & editing. **X.Z.** : Investigation, Writing-review & editing. **F.Z**: Writing-review & editing. **B.Y.** : Supervision, Investigation, Conceptualization, Writing-review & editing. **Z.Z.** : Supervision, Investigation, Writing-review & editing. **Y.W.** : Supervision, Investigation, Writing-review & editing. **H.Y**: Supervision, Investigation, Writing-review & editing. **J.L**: Investigation,

Writing-review & editing. **J.L.** : Investigation, Writing-review & editing. **M.H**: Investigation, Writing-review & editing. **J.T**: Investigation, Writing-review & editing. **C.W.** : Investigation, Writing-review & editing. All authors approved the final version of the manuscript and agreed to be accountable for all aspects of the work in ensuring that questions related to the accuracy or integrity of any part of the work are appropriately investigated and resolved.

Data availability statement

Date can be found at Mendeley Data, available at the following URL: https://doi.org/10.17632/84gkydb5y9.1

Additional Information

Supplementary Files

This is a list of supplementary files associated with this preprint. Click to download.

- TableS1.xlsx
- TableS2.xlsx
- TableS3.xlsx
- TableS4.xlsx